https://dx.doi.org/10.1016/j.engstruct.2019.109441

Dynamic characteristics of functionally graded porous beams with interval material properties

Kang Gao [a], Ruilong Li [b], Jie Yang [a*]

[a] School of Engineering, RMIT University, PO Box 71, Bundoora, VIC 3083 Australia

[b] Department of Civil and Environmental Engineering, The Hong Kong Polytechnic University, Hung Hom, Kowloon, Hong Kong, China

Graphical abstract

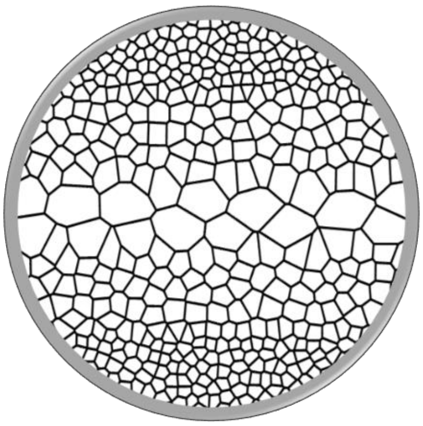

Type 1 Symmetric porosity distribution 1

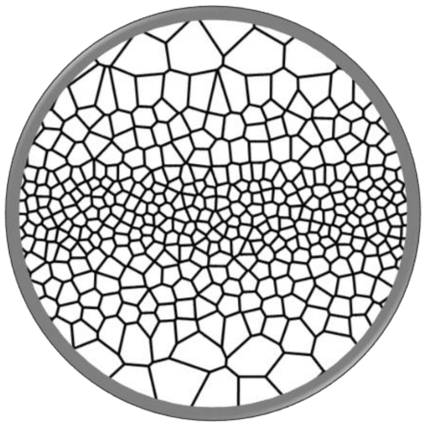

Type 2 Symmetric porosity distribution 2

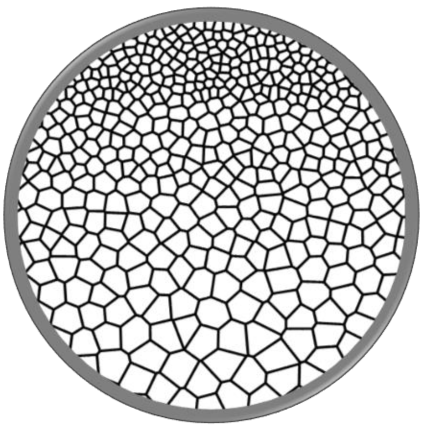

Type 3 Non-symmetric porosity distribution

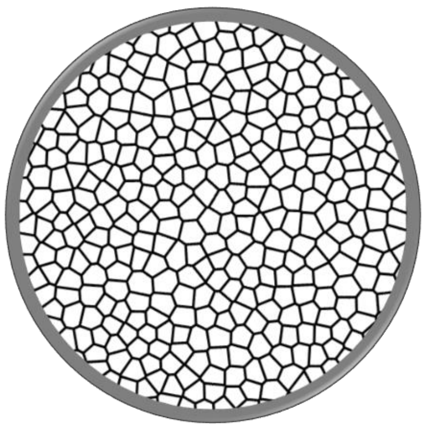

Type 4 Uniform porosity distribution

Declarations of interest: none

* Corresponding author: j.yang@rmit.edu.au (J. Yang)

Abstract

This paper presents a new computational approach named hybrid Chebyshev surrogate model with discrete singular convolution (CSM-DSC) method to study the nondeterministic dynamic characteristics of functionally graded (FG) porous beams with material uncertainties. In the proposed approach, interval analysis can be directly applied in hybrid CSM-DSC computational framework, then the upper and low bounds of the dynamic responses of FG porous beams with various boundary conditions can be readily obtained. Based on Hamilton's principle and Timoshenko beam theory, the governing equation is established and solved by DSC method. By utilizing the higher-dimensional Chebyshev surrogate (HDCS) model, the approximate performance function involving uncertainty in three critical material properties, such as Young's modulus, mass density and porosity coefficient, is developed numerically. In order to verify the validity and accuracy of the proposed method, deterministic analysis and nondeterministic analysis are implemented to compare the present results against the published ones, and those obtained by the finite element method (FEM) and quasi-Monte Carlo simulation (QMCS) method. A comprehensive parametric study is then conducted to examine the influences of material parameter uncertainties, porosity distribution patterns, porosity coefficient, boundary conditions, and aspect ratio on the bounds of frequencies. The results show that the uncertainty of Young's modulus has the most significant effect on beam's dynamic responses, followed by that of mass density whereas the influence of the uncertain of porosity coefficient is much less pronounced.

Keywords

Functionally graded porous structures; dynamic characteristics; Chebyshev surrogate model; discrete singular convolution; interval analysis.

1. Introduction

It is known that the density of cortical region is larger than that of trabecular region in femur [1]. Such non-uniform or graded density in bone can optimize the overall mechanical performance of the skeletal structures. This has also been found in microcellular plant structures such as wood, bamboo and some plant stems [2]. Inspired by these natural phenomena, the functionally graded metallic foam was fabricated and soon became very popular material in both research and industry communities. Previous researches on functionally graded porous materials demonstrated that they have outstanding impact energy absorption, high strength-weight ratio, excellent energy-efficiency, as well as low thermal conductivity, advantageous damping and acoustical absorptivity properties. Owing to their superior and unique material properties, FG porous materials have found a wide range of applications in electronics, biomedical, aerospace, civil and automotive engineering.

Extensive analytical, numerical and experimental works on various static and dynamic behaviors such as static bending[3, 4], free and forced vibrations[5, 6], elastic buckling and postbuckling[3, 7, 8], and dynamic stability for FG structures[5, 9-12], especially for porous structures have been conducted these years. Chen et al. [3] studied the effect of different porosity distributions on buckling, bending, and free and forced vibrations of FG porous beams under a harmonic point load, an impulsive point load and a moving load with constant velocity. The nonlinear dynamic buckling of FG porous beams was presented by Gao et al. [12] based on analytical-numerical method and finite element method. Numerical results for four different types of FG porosity patterns including two symmetric, one non-symmetric and uniform porosity distributions were presented. Gao et al. [13] employed Galerkin technique and multiple scales method in nonlinear primary resonance analysis of FG porous cylindrical shells. Ziane et al.[14] presented the thermal buckling of FG porous box beams with simply supported and clamped-clamped boundary conditions. Most recently, nanocomposite metal foams have been successfully synthesized and attracted considerable research attention [15-21]. Kitipornchai and his co-workers [22] made the first attempt to study the buckling and free vibration characteristics of FG porous nanocomposite beams reinforced by graphene platelets (GPLs) that are non-uniformly dispersed in metal matrix. Following this pioneering work, Chen et al. [7] investigated the combined effects of different porosity distribution and GPLs distribution patterns on the vibration and postbuckling behaviors of FG porous nanocomposite beams. The bending and thermal buckling behaviours of FG-GPLs laminated beams was investigated by Shen et al.[4]. By employing the differential quadrature method, Gao et al. [23] studied the nonlinear free vibration of GPL reinforced FG porous nanocomposite plates with various boundary conditions and found that porosity distribution plays a more important role than GPL dispersion pattern.

It should be mentioned that almost all of the existing investigations on FG porous structures are deterministic in which all material parameters such as Young's modulus, mass density, porosity coefficients, etc., are assumed to be deterministic constants. The success of such analyses is largely underpinned by predetermined material and geometric properties as well as reasonable assumptions. However, the presence of uncertainty, unpredictability and randomness in system parameters at different levels is inevitable due to various errors in fabrication and manufacturing processes, especially for functionally graded materials whose manufacturing is far from mature. Ghasemi et al. [23] discussed the metamodel-based probabilistic optimization of CNT/polymer composite structures in the framework of stochastic multi-scale material model and a kriging metamodel. Their study showed that deterministic methods for nanocomposite modelling and optimization may lead to erroneous results in certain cases. The metamodel-based approach was also used by García-Macías et al. [24] in the analysis of FG carbon nanotubes (CNTs) reinforced plates with random CNT distributions and materials parameters. Dey et al. [25] presented the random sampling-high dimensional model representation (RS-HDMR) method to discuss the stochastic free vibration analysis of angle-ply composite plates. It has been well accepted that probabilistic structural analysis based on the complete statistical information of the stochastic systems and the corresponding probability distributions is capable of producing more accurate results. Unfortunately, such complete statistical information and probability distributions are either almost impossible or extremely expensive to obtain in reality. This calls for the non-probabilistic approaches, for example, fuzzy method, interval analysis and convex model, to name but just a few, as the alternative methods for practical use. Gao et al. [26] proposed the Chebyshev surrogate model to study the upper and lower bounds of dynamic buckling responses of Euler-Bernoulli beams. Wu et al. [27] employed the finite element method in static analysis of FG structures with interval variables. Under the similar framework, they [28] investigated the linear elastic problem of FG porous beam structures with material, geometrical and loading uncertainties. The mechanical behaviour of a 3D heterogenous materials with uncertain-but-bounded parameters was analysed by Ma et al. [29]. All these studies revealed that the interval-based uncertainty procedures can obtain reliable upper and lower bounds from the uncertain-but-bounded parameters with significantly improved computational efficiency.

Although rapidly developed manufacturing techniques make the production of FG porous materials possible, it is still very difficult to manufacture such materials according to the intended design distributions. This attributes to the fact that experimental results sometimes do not match preconceived expectations of theoretical simulations. On the other hand, due to the inherent and random complexity in fabrication process, the mechanical properties of the FG porous materials, especially the Young's modulus, mass density and porosity coefficients, are not deterministic in nature. Therefore, the nondeterministic analysis of FG porous structures is an important topic that requires urgent attention due to its practical significance. However, to the best of the authors' knowledge and as can be seen from the above literature review, no previous work has been done on the dynamic characteristics of FG porous structures with uncertainty material properties.

To fill in this research gap, a novel nondeterministic dynamic analysis of shear deformable FG porous beams using Chebyshev surrogate method is proposed in this paper to investigate the upper and lower bounds of dynamic responses. Both frequencies and mode shapes of the FG porous beams with material uncertainties are studied by interval analysis. Firstly, discrete singular convolution (DSC) method in conjunction with the Hamilton's principle is employed to obtain eigenvalue equation for deterministic analysis. Based on the Chebyshev interpolation series, the interpolation points of each interval material parameter are created. By inputting all observation points into analytical-numerical solution, the outcome of interest is obtained. Then the approximate performance function is established between inputs and outputs with all the interval variables through the higher-dimensional Chebyshev surrogate (HDCS) model. The effectiveness and validity of the proposed method are thoroughly examined by two steps: deterministic analysis and nondeterministic analysis. For deterministic analysis, the accuracy of the presented method is verified against the results of other authors and finite element method; As for nondeterministic analysis, the efficacy of the HDCS model is compared with quasi-Monte Carlo simulations (QMCS) method. Finally, a detailed parametric analysis is conducted to study the influence of porosity distribution patterns, porosity coefficient, boundary conditions, aspect ratio on the bounds of frequencies as well as the influence of material parameters with various uncertainty degrees.

2. Material properties of functionally graded beams

Fig.1 shows a simply supported Timoshenko beam made of different types of porosity distributions, where w_0 denotes the structural deflection of the beam. The Cartesian coordinate system (x, y, z) is established, in which the (x, y) plane is on the middle surface of the beam and z is the thickness direction.

In this case, four types of FG porous distributions, namely Type 1 (symmetric porosity distribution which is stiffer in surface areas)[3, 6, 7, 12, 13, 23, 30], Type 2 (symmetric porosity distribution which is softer in surface areas), Type 3 (non-symmetric porosity distribution) [31-

35], and Type 4 (uniform porosity distribution) are considered, as shown in Fig.2. The mathematic models of Young's modulus $E(z)$, shear modulus $G(z)$ and mass density $\rho(z)$ for the four different porous distributions can be described by Eq.(1)

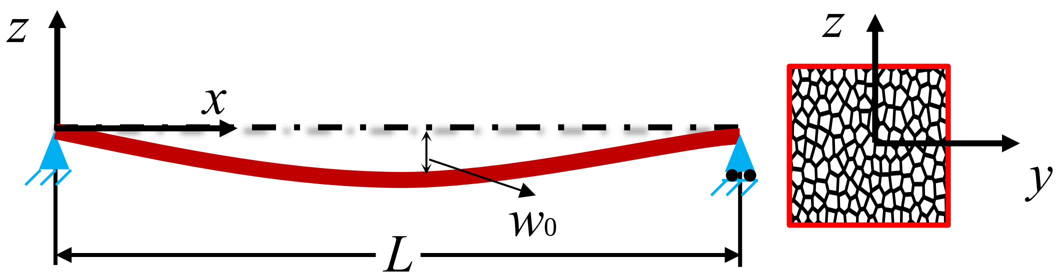

Fig.1 A simply supported Timoshenko beam made of metal foams

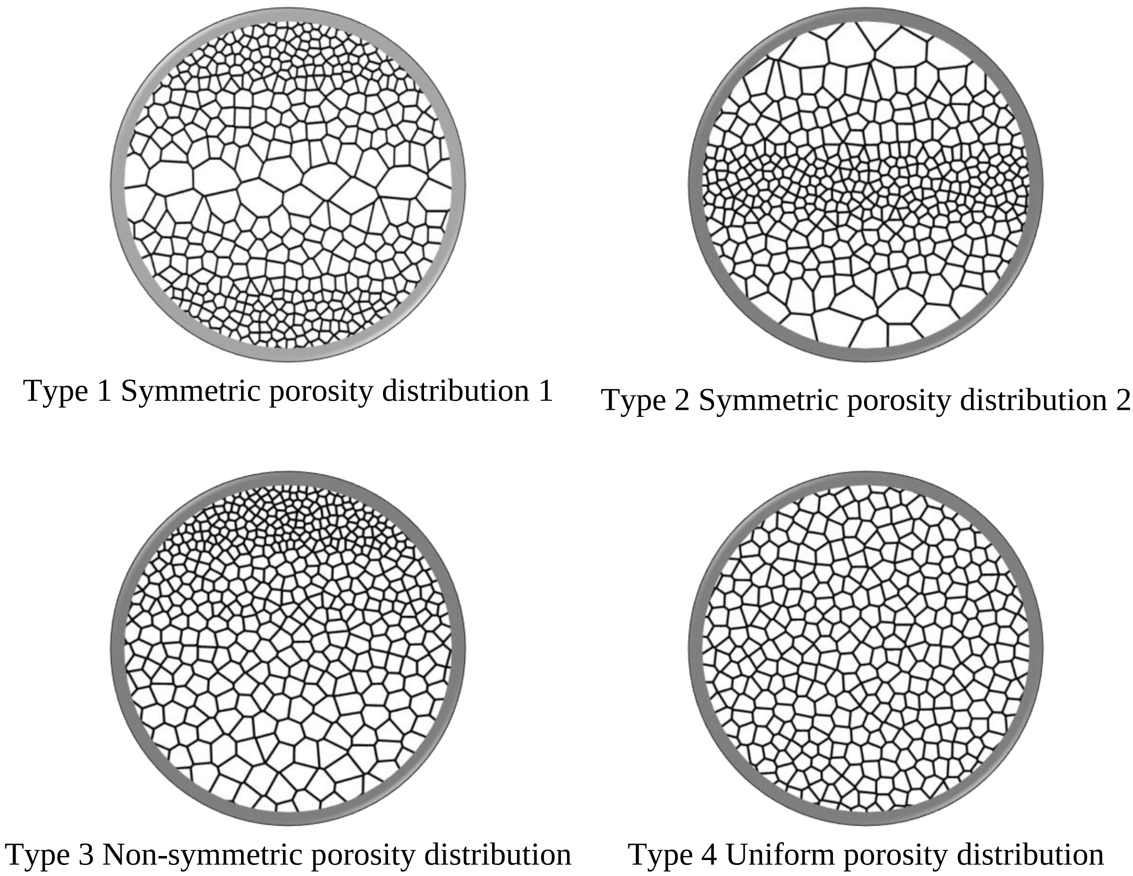

Fig.2 Cross-section of the FG porous beams with different porosity distributions

$$
\begin{aligned}
E(z) &= E_{\max}\left[1 - N_0\varphi(z)\right] \\
G(z) &= G_{\max}\left[1 - N_0\varphi(z)\right] \\
\rho(z) &= \rho_{\max}\left[1 - N_m\varphi(z)\right]
\end{aligned}
\tag{1}
$$

where

$$\varphi(z)=\begin{cases}\cos\left(\dfrac{\pi z}{h}\right) & T1\\ \cos\left(\left|\dfrac{\pi z}{h}\right|-\dfrac{\pi}{2}\right) & T2\\ \cos\left(\dfrac{\pi z}{2h}+\dfrac{\pi}{4}\right) & T3\\ \varphi_0 & T4\end{cases} \tag{2}$$

where E_{max}, G_{max} and ρ_{max} are the maximum values of Young's modulus, shear modulus and mass density, respectively. h is the thickness of the beam and varies from $-h/2$ to $h/2$. N_0 is the porosity coefficient and can be obtained by $N_0 = 1 - E_{min}/E_{max} = 1 - G_{min}/G_{max}$. E_{min}, G_{min} and ρ_{min} are the corresponding minimum values.

For an open-cell metal foam, the relationship between Young's modulus and mass density can be expressed [36]

$$\frac{E_{\min}}{E_{\max}}=\left(\frac{\rho_{\min}}{\rho_{\max}}\right)^2 \tag{3}$$

Consequently, one can obtain the expression between N_m and N_0

$$N_m = 1-\sqrt{1-N_0} \tag{4}$$

3. Deterministic analysis of free vibration of FG porous beams

3.1.Equations of motion

Due to the limitation of classic beam theory on estimating the natural frequency and mode shape of multilayer or sandwich composite structures, several shear deformation theories have been presented in past decades. To derive the equations of motion or governing equations of FG porous beams, the Timoshenko beam theory is used in this study to consider the importance of shear deformation and rotary inertia effects.

$$\begin{aligned} u(x,z,t) &= u_0(x,t)+z\varphi(x,t)\\ w(x,z,t) &= w_0(x,t) \end{aligned} \tag{5}$$

where u and w are the displacements of any point in the beam along axes x and z; u_0 and w_0 are the displacement components at the mid-surface of the beam. φ is the section rotation about the x axis. The strain-displacement relationship derived from above equations can be expressed as:

$$\varepsilon_{xx} = \frac{\partial u_0}{\partial x} + z\frac{\partial \varphi}{\partial x}$$
$$\gamma_{xz} = \frac{\partial w_0}{\partial x} + \varphi \tag{6}$$

where ε_{xx} and γ_{xz} are the normal strain and shear strain, respectively. Then the corresponding normal stress σ_{xx} and shear stress τ_{xz} can be derived as

$$\sigma_{xx} = Q_{11}(z)\varepsilon_{xx}, \quad \tau_{xz} = Q_{55}(z)\gamma_{xz} \tag{7}$$

where

$$Q_{11}(z) = \frac{E(z)}{1-\nu^2}, \quad Q_{55}(z) = G_{12} = \frac{E(z)}{2(1+\nu)} \tag{8}$$

According to Hamilton's principle[10], the equations of motion for vibration analysis of FG porous beams can be obtained as

$$\frac{\partial N_x}{\partial x} = I_0\frac{\partial^2 u_0}{\partial t^2} + I_1\frac{\partial^2 \varphi}{\partial t^2} \tag{9}$$
$$\frac{\partial M_x}{\partial x} - Q_x = I_1\frac{\partial^2 u_0}{\partial t^2} + I_2\frac{\partial^2 \varphi}{\partial t^2}$$
$$\frac{\partial Q_x}{\partial x} = I_0\frac{\partial^2 w_0}{\partial t^2}$$

where N_x, M_x and Q_x are the stress resultants for axial force, bending moment and shear force, respectively, which are expressed as

$$N_x = A_{11}\frac{\partial u_0}{\partial x} + B_{11}\frac{\partial \varphi}{\partial x}$$
$$M_x = B_{11}\frac{\partial u_0}{\partial x} + D_{11}\frac{\partial \varphi}{\partial x} \tag{10}$$
$$Q_x = \kappa A_{55}\left(\frac{\partial w_0}{\partial x} + \varphi\right)$$

where κ denotes the shear correction factor and is taken κ=5/6. And A_{11}, B_{11}, D_{11} and A_{55} are the material stiffness components of FG porous beams and are defined as

$$\left(A_{11}, B_{11}, D_{11}\right) = \int_{-h/2}^{h/2} Q_{11}(z)\left(1, z, z^2\right)dz$$
$$A_{55} = \int_{-h/2}^{h/2} Q_{55}(z)dz \tag{11}$$

And the inertia terms in the Eq.(9) can be written as

$$\left(I_0, I_1, I_2\right) = \int_{-h/2}^{h/2} \rho(z)\left(1, z, z^2\right)dz \tag{12}$$

By substituting Eq.(10) into Eq.(9), the governing equation can be rewritten as

$$
\begin{aligned}
&A_{11}\frac{\partial^2 u_0}{\partial x^2}+B_{11}\frac{\partial^2 \varphi}{\partial x^2}=I_0\frac{\partial^2 u_0}{\partial t^2}+I_1\frac{\partial^2 \varphi}{\partial t^2}\\
&B_{11}\frac{\partial^2 u_0}{\partial x^2}+D_{11}\frac{\partial^2 \varphi}{\partial x^2}-\kappa A_{55}\left(\frac{\partial w_0}{\partial x}+\varphi\right)=I_1\frac{\partial^2 u_0}{\partial t^2}+I_2\frac{\partial^2 \varphi}{\partial t^2}\\
&\kappa A_{55}\left(\frac{\partial^2 w_0}{\partial x^2}+\frac{\partial \varphi}{\partial x}\right)=I_0\frac{\partial^2 w_0}{\partial t^2}
\end{aligned}
\tag{13}
$$

3.2.Solution procedures

There are several analytical and numerical methods for the dynamic analysis of shear deformation beams, such as the method of differential quadrature (DQ), discrete singular convolution (DSC), Chebyshev collocation method and FE method. Compared to other numerical methods, DSC method can obtain not only accurate lower mode frequencies but also accurate higher mode frequencies[37, 38]. At the same time, DSC is an efficient method for analysing the challenge problems, like free boundary conditions or discontinuities in geometry or load. Thus the DSC method is utilized to investigate the dynamic characteristics of FG porous beams with different boundary conditions. According to the conception of DSC, for a one-dimensional function *f*(*x*), the *n*th-order derivative with respect to *x* can be approximated as

$$
\left.\frac{d^n f(x)}{dx^n}\right|_{x=x_i}=f^{(n)}(x)\approx\sum_{k=-M}^{M}\delta_{\sigma,\Delta}^{(n)}(x_i-x_k)f(x_k)\qquad(n=0,1,2...)
\tag{14}
$$

where x_i is the specific central point and x_k are the set of discrete grid points that surround the point x_i. $2M+1$ is the effective kernel, or computational bandwidth; and $\delta_{\sigma,\Delta}(x_i-x_k)$ is a symbol for the delta kernels of Dirichlet type.

As Wei et al [39] stated, there are several different approximation kernels, while the use of the regularized Shannon kernel (RSK) is very efficient due to its small truncation errors. And the definition of regularized Shannon kernel is given as

$$
\delta_{\sigma,\Delta}(x-x_k)=\frac{\sin\left[(\pi/\Delta)(x-x_k)\right]}{(\pi/\Delta)(x-x_k)}\exp\left[-\frac{(x-x_k)^2}{2\sigma^2}\right]
\tag{15}
$$

The *n*th derivative of $\delta_{\sigma,\Delta}(x-x_k)$ can be expressed as

$$
\delta_{\sigma,\Delta}^{(n)}(x-x_k)=\left(\frac{d}{dx}\right)^n\delta_{\sigma,\Delta}\left(x-x_k\right)
\tag{16}
$$

where Δ is the grid spacing between two grid points and σ is the parameter that influenced by grid spacing and determine the computational accuracy.

In order to maintain the readability of the paper by efficiently expressing all formulations, the following dimensionless quantities are necessarily introduced:

$$\begin{aligned}
&\xi=\frac{x}{L},(u,w)=\frac{(u_0,w_0)}{h},\eta=\frac{L}{h},\\
&(\bar{I}_0,\bar{I}_1,\bar{I}_2)=\left(\frac{I_0}{I_{10}},\frac{I_1}{I_{10}h},\frac{I_2}{I_{10}h^2}\right),\\
&(a_{11},a_{55},b_{11},d_{11})=\left(\frac{A_{11}}{A_{110}},\frac{A_{55}}{A_{110}},\frac{B_{11}}{A_{110}h},\frac{D_{11}}{A_{110}h^2}\right),\\
&\tau=\frac{t}{L}\sqrt{\frac{A_{110}}{I_{10}}},\omega=\Omega L\sqrt{\frac{I_{10}}{A_{110}}}
\end{aligned}\tag{17}$$

where I_{10} and A_{110} are the values of I_0 and A_{11} of a homogenous beam made from pure materials. The governing Eq.(13) can be transformed into the following dimensionless forms

$$\begin{aligned}
&a_{11}\frac{\partial^2 u}{\partial\xi^2}+b_{11}\frac{\partial^2\varphi}{\partial\xi^2}=\bar{I}_0\frac{\partial^2 u}{\partial\tau^2}+\bar{I}_1\frac{\partial^2\varphi}{\partial\tau^2}\\
&\kappa a_{55}\left(\frac{\partial^2 w}{\partial\xi^2}+\eta\frac{\partial\varphi}{\partial\xi}\right)=\bar{I}_0\frac{\partial^2 w}{\partial\tau^2}\\
&b_{11}\frac{\partial^2 u}{\partial\xi^2}+d_{11}\frac{\partial^2\varphi}{\partial\xi^2}-\kappa\eta a_{55}\left(\frac{\partial w}{\partial\xi}+\eta\varphi\right)=\bar{I}_1\frac{\partial^2 u}{\partial\tau^2}+\bar{I}_2\frac{\partial^2\varphi}{\partial\tau^2}
\end{aligned}\tag{18}$$

For the vibration analysis of FG porous beams, the displacements can be defined as

$$\begin{aligned}
u(\xi,\tau)&=U(\xi)e^{-i\omega\tau}\\
w(\xi,\tau)&=W(\xi)e^{-i\omega\tau}\\
\varphi(\xi,\tau)&=\psi(\xi)e^{-i\omega\tau}
\end{aligned}\tag{19}$$

where $i=\sqrt{-1}$ and ω is the dimensionless natural frequency.

By substituting Eq.(19) into the equation of motions (18), and then applying the DSC-rules of Eq.(15) and (16), then following relations can be obtained

$$\begin{aligned}
&a_{11}D2U+b_{11}D2\psi=-\bar{I}_0\omega^2U_k-\bar{I}_1\omega^2\psi_k\\
&\kappa a_{55}\left(D2W+\eta D1\psi\right)=-\bar{I}_0\omega^2W_k\\
&b_{11}D2U+d_{11}D2\psi-\kappa\eta a_{55}\left(D1W+\eta\psi_k\right)=-\bar{I}_1\omega^2U_k-\bar{I}_2\omega^2\psi_k
\end{aligned}\tag{20}$$

where D1(·) and D2(·) are operators of DSC for different displacement components. For example, the first-order and second-order derivatives of $U(\xi)$ based on RSK can be approximated as follows

$$\begin{aligned} D1U &= \frac{dU(\xi_i)}{d\xi} \approx \sum_{k=-M}^{M} \frac{d}{d\xi}\left[\delta_{\sigma,\Delta}(\xi-\xi_{i+k})\right]\Big|_{\xi=\xi_i} \bullet U_{i+k} \\ &= \sum_{k=-M}^{M} \delta_{\sigma,\Delta}^{(1)}(k\Delta) \bullet U_{i+k} \\ D2U &= \frac{d^2U(\xi_i)}{d\xi^2} \approx \sum_{k=-M}^{M} \frac{d^2}{d\xi^2}\left[\delta_{\sigma,\Delta}(\xi-\xi_{i+k})\right]\Big|_{\xi=\xi_i} \bullet U_{i+k} \\ &= \sum_{k=-M}^{M} \delta_{\sigma,\Delta}^{(2)}(k\Delta) \bullet U_{i+k} \end{aligned} \tag{21}$$

For FG porous beam with different boundary conditions, the requirements on the boundary can be given as:

$$\begin{aligned} &Pinned(P): U = W = b_{11}\frac{\partial U}{\partial \xi} + d_{11}\frac{\partial \psi}{\partial \xi} = 0 \\ &Clamped(C): U = W = \psi = 0 \\ &Free(F): \begin{cases} a_{11}\dfrac{\partial U}{\partial \xi} + b_{11}\dfrac{\partial \psi}{\partial \xi} = 0 \\ \dfrac{\partial W}{\partial \xi} + \eta\psi = 0 \\ b_{11}\dfrac{\partial U}{\partial \xi} + d_{11}\dfrac{\partial \psi}{\partial \xi} = 0 \end{cases} \end{aligned} \tag{22}$$

Applying appropriate boundary conditions to Eq.(20), one can obtain the general form of eigenvalue equation as follows:

$$[\boldsymbol{D}]\{\boldsymbol{Y}\} = \boldsymbol{\Omega}^2[\boldsymbol{M}]\{\boldsymbol{Y}\} \tag{23}$$

where $\boldsymbol{D}$ is the stiffness matrix and $\boldsymbol{M}$ is the associated mass matrix. $\boldsymbol{Y}=\{U_0,U_1,\ldots,U_{N-1},W_0,W_1,\ldots,W_{N-1},\psi_0, \psi_1,\ldots,\psi_{N-1}\}^{\mathrm{T}}$, and $\mathbf{\Omega}=\mathrm{diag}\{\omega_0, \omega_1, \ldots,\omega_{N-1}\}$.

3.3.Verification and accuracy of the deterministic analysis

According to the deterministic analysis method discussed above, the accuracy, applicability of the presented method for vibration analysis of FG porous beams is studied in this section. To maintain the least truncation error for interpolation and numerical differentiation, a mathematical estimation for relationship between σ, Δ and M was proposed by Qian and Wei[40], as shown below.

$$r(\pi - B\Delta) > \sqrt{2\ln 10 \times \varepsilon}, \quad \frac{M}{r} > \sqrt{2\ln 10 \times \varepsilon} \tag{24}$$

where r is discretization parameter, which equals to σ/Δ ; Δ is the grid spacing between two grid points and σ is the parameter that influenced by grid spacing and determine the computational accuracy; B is the frequency bound for the function of interest; ε is the desired order of accuracy. For example, if r=3, the calculation accuracy of the target function approaches to ε=15 when M=30;

Before calculating the results of natural frequencies of FG beams with different boundary conditions, the very first step is do a convergence study and find the optimal M and r to maintain the accuracy and efficiency of the proposed method. Fig.3 shows the convergence curve of the dimensionless natural frequencies of FG beams. The power law (PL) distribution of FG beams is considered[41]. The material properties are E_c=380 GPa, ρ_c=3960kg/m^3, v_c=0.3 for Al_2O_3 and E_m=70 GPa, ρ_m=2702kg/m^3, v_m=0.3 for Al. The clamped-clamped (C-C) boundary condition is studied. As an example, in Fig.3, for a given grid points M=30, the results converge to 7.9081 with r from 7 to 12. The authors did the convergence study for all the power law (PL) distributions with different boundary conditions and found that the figures are almost the same. Therefore, to keep the readability of the study, the authors just keep one typical example here. And more convergence study about DSC method can be found in [37, 38]. Meanwhile, a set of DSC parameters, which satisfies the convergence for different material properties, geometrical properties and boundary conditions, can be selected by utilizing the convergence curves.

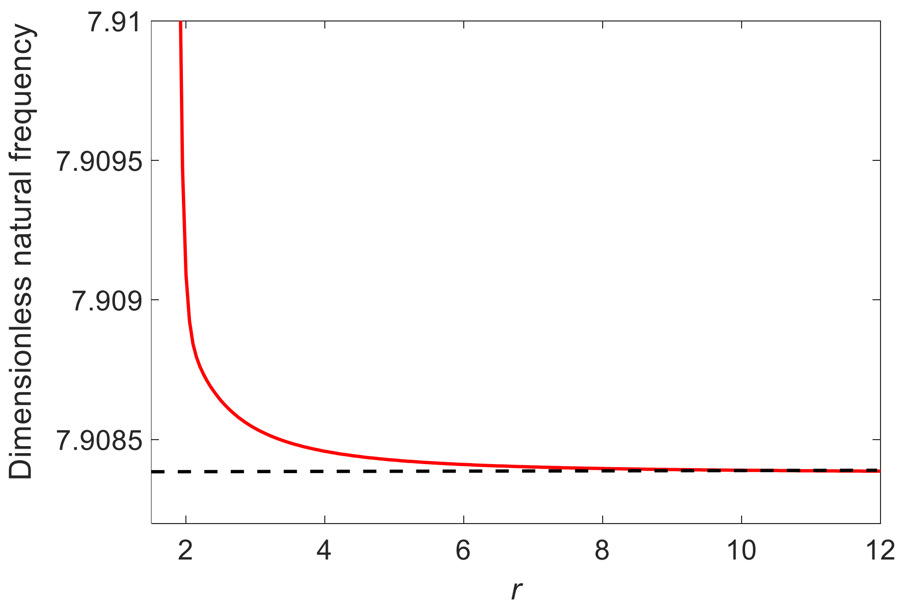

Fig.3 The convergence study of the dimensionless natural frequencies of FG beams (η=5, n=1 with C-C boundary condition)

After the convergence study of present method, the proposed method is verified with Wattanasakulpong and Mao [41] by using the Chebyshev collocation method and Şimşek [42] by using the Lagrange multiplier method. The comparison of the dimensionless fundamental frequencies from present method and other methods in open literature is shown in table.1. As can be seen, the proposed method matches very well for all different aspect ratios η and the material volume fraction indexes n.

Table. 1 The dimensionless fundamental frequencies $\omega = \left(\Omega L^2 / h\right)\sqrt{\rho_m / E_m}$ of FGM-PL beams from present method, Wattanasakulpong [41] and Şimşek [42]

η	Method	n=0	n=0.5	n=1.0	n=2.0	n=5.0
5	Present	10.0000	8.6724	7.9081	7.1896	6.6445
	Wattanasakulpong [41]	9.9975	8.6705	7.8998	7.1880	6.6428
	Şimşek [42]	10.0344	8.7005	7.9253	7.2113	6.6676
20	Present	12.2204	10.4230	9.4294	8.6022	8.1677
	Wattanasakulpong [41]	12.2201	10.4228	9.4292	8.6020	8.1675
	Şimşek [42]	12.2235	10.4263	9.4314	8.6040	8.1698
30	Present	12.3355	10.5115	9.5059	8.6733	8.2478
	Wattanasakulpong [41]	12.3354	10.5114	9.5058	8.6733	8.2477
50	Present	12.3958	10.5577	9.5458	8.7105	8.2898
	Wattanasakulpong [41]	12.3958	10.5577	9.5458	8.7105	8.2898
100	Present	12.4215	10.5774	9.5628	8.7264	8.3078
	Wattanasakulpong [41]	12.4215	10.5774	9.5628	8.7264	8.3077

Table. 2 The first three dimensionless frequencies $\omega = \Omega L\sqrt{I_{00} / A_{110}}$ of FGM-PL beams for various material models and boundary conditions

Material model	Mode	P-P		C–C		C-P		C–F	
		Present	Wattanasakulpong [41]	Present	Wattanasakulpong [41]	Present	Wattanasakulpong [41]	Present	Wattanasakulpong [41]
FGM-PL	ω_1	0.4460	0.4448	0.9048	0.9048	0.6326	0.6453	0.1493	0.1493
	ω_2	1.5876	1.5883	2.3364	2.3360	1.9580	1.9612	0.8987	0.8987
	ω_3	3.3975	3.3975	4.2523	4.2510	3.8345	3.8051	2.3744	2.3742
FGM-EX	ω_1	0.4206	0.4188	0.8344	0.8343	0.5804	0.5977	0.1379	0.1379
	ω_2	1.4608	1.4618	2.1502	2.1498	1.8025	1.8072	0.8289	0.8288
	ω_3	3.1314	3.1311	3.9057	3.9045	3.5287	3.4937	2.1839	2.1837
FGM-MT	ω_1	0.4106	0.4042	0.8160	0.8062	0.5683	0.5777	0.1351	0.1335
	ω_2	1.4293	1.4131	2.0994	2.0739	1.7620	1.7449	0.8111	0.8014
	ω_3	3.0587	3.0219	3.8080	3.7610	3.4449	3.3683	2.1328	2.1070

Table.2 shows the results of present method and Wattanasakulpong [41] for the first three dimensionless frequencies from different mathematical models of functionally graded materials, like FGM-PL (power law distribution), FGM-EX (exponential distribution) and FGM-MT (Mori-Tanaka scheme). It is clear that the proposed method has a good agreement with Wattanasakulpong [41] for all the numerical cases.

Table. 3 The dimensionless natural frequencies from present method, Chen et al.[6] and FEM for different aspect ratios and boundary conditions

	T1			T3		
L/h	Present	Chen et al.[6]	FEM	Present	Chen et al.[6]	FEM
			P-P			
10	0.2798	0.2798	0.2778	0.2599	0.2599	0.2549
20	0.1422	0.1422	0.1419	0.1320	0.1318	0.1296
50	0.0571	0.0571	0.0571	0.0569	0.0529	0.0521
			C-C			
10	0.5945	0.5944	0.6101	0.5475	0.5475	0.5600
20	0.3166	0.3166	0.3176	0.2888	0.2888	0.2941
50	0.1291	0.1291	0.1289	0.1174	0.1174	0.1183
			C-P			
10	0.4246	0.4242	0.4227	0.3875	0.3898	0.3905
20	0.2205	0.2203	0.2201	0.1995	0.2013	0.2015
50	0.0892	0.0891	0.0891	0.0793	0.0813	0.0813
			C-F			
10	0.1008	0.1008	0.1007	0.0917	0.0917	0.0920
20	0.0508	0.0508	0.0508	0.0462	0.0462	0.0463
50	0.0204	0.0204	0.0204	0.0185	0.0185	0.0186

Furthermore, the proposed method is validated with results of Chen et al. [6] and finite element method for FG porous beams with different aspect ratios and boundary conditions, as stated in Table.3. Both T1 and T3 are investigated in present model. In the end, the accuracy of the present method is thoroughly studied by comparing with cited references and other methods from different cases. Obviously, excellent agreement can be obtained from present method.

3.4.Parametric study of the deterministic analysis

In this subsection, a detailed parametric study of FG porous beams is carried out based on the deterministic analysis. Dynamic characteristics of FG porous beams, by considering different porosity coefficients N_0, distribution types, boundary conditions and aspect ratios, are comprehensively discussed. The material properties of the metal foam are: E=200GPa, v=1/3, ρ=7850kg/m^3. The geometrical parameters of the rectangular beam are h=0.1m, L=1 m.

Fig.4 plots the dimensionless natural frequency of FG porous beams for various porosity coefficients, boundary conditions and distribution patterns. The following conclusions can be made from this figure: 1. T1 possesses the maximum frequencies while T2 is the least one; The differences between T3 and T4 were much less pronounced; 2. C-C boundary has the largest frequencies, then C-P and P-P, the frequency of C-F boundary conditions is the least; 3. Except T1, the frequencies of all the other distributions decrease with the increase of void fraction or porosity. The reason of this phenomenon is that although both mass and stiffness are linearly decrease with the increase of porosity coefficients, the pace of mass declines is lower than that of stiffness[23].

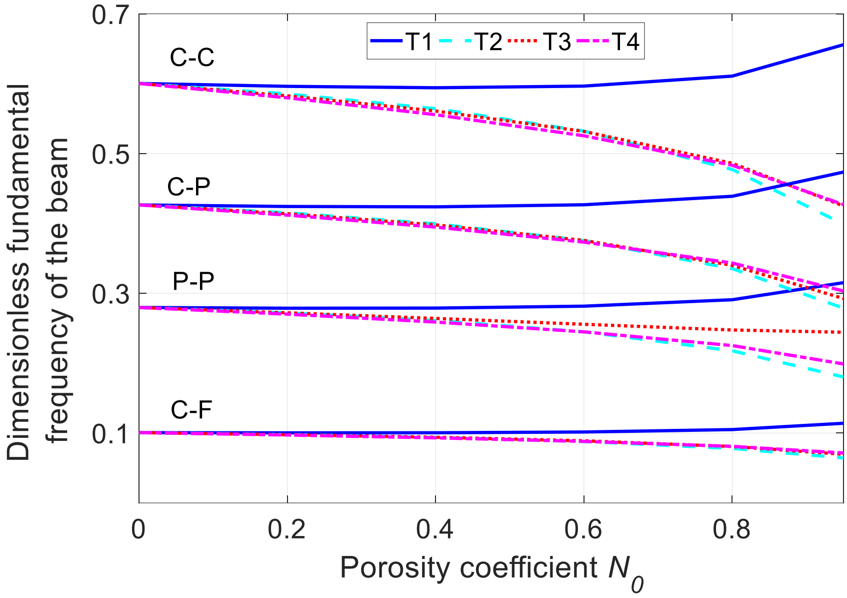

Fig.4 The influence of porosity coefficient N_0 on different types of distributions and boundary conditions

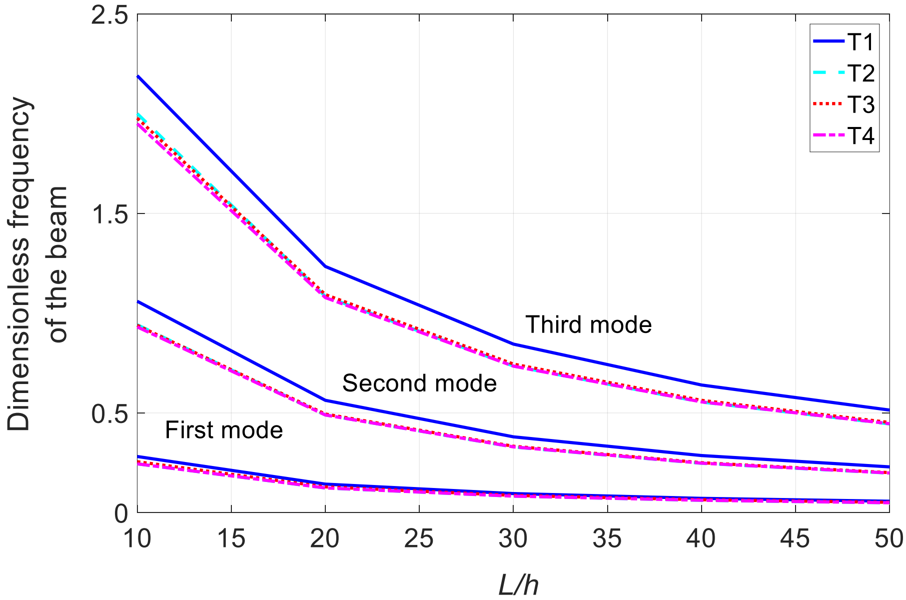

Fig.5 The influence of aspect ratios L/h on frequencies of the first three modes for different types of distributions with P-P boundary condition

The frequencies of the first three modes for different L/h, distribution types with P-P boundary condition are given in Fig.5. five different η are selected, such as 10, 20, 30, 40 and 50. The porosity coefficient equals to 0.6 in this figure. For different natural frequencies, the frequencies decrease dramatically with the increase of L/h ratios. Similarly, T1 has the largest frequencies while frequencies of other three patterns are almost the same.

Fig.6 shows the mode shape of T1 along u, w and ϕ_0 directions with P-P boundary condition. The material properties and the geometrical parameters are same as before. The first ten mode shapes are studied. One interesting finding is that for different FG porous types and boundary conditions, the mode shape jump phenomena might be different. For example, for T1-P-P, the 4, 7 and 10 mode jumps to longitudinal direction and there is no vibration along transverse and rotation directions, as shown in Fig.6(1). While for other modes, both transverse and rotation are concurrence and no axial deformation modes.

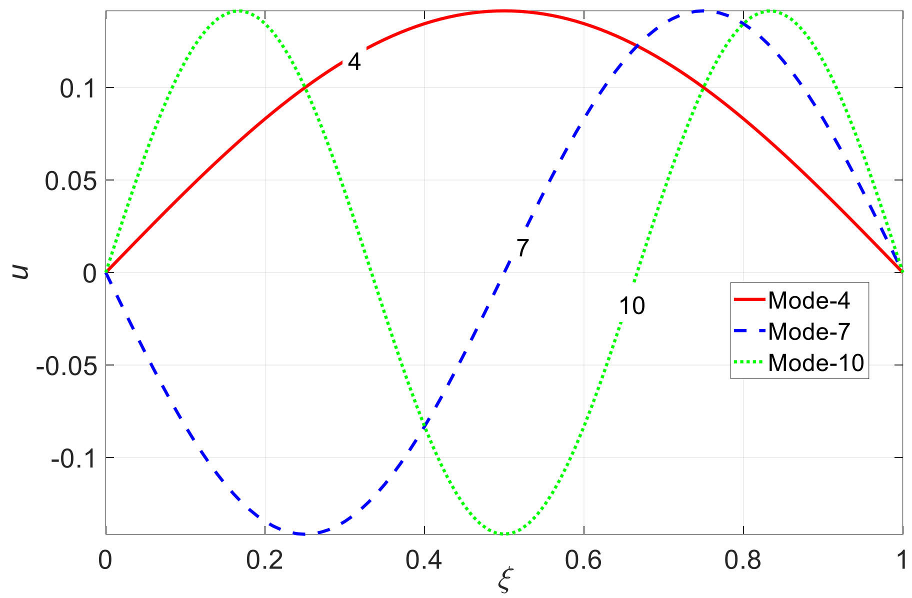

(1) Longitudinal vibration modes

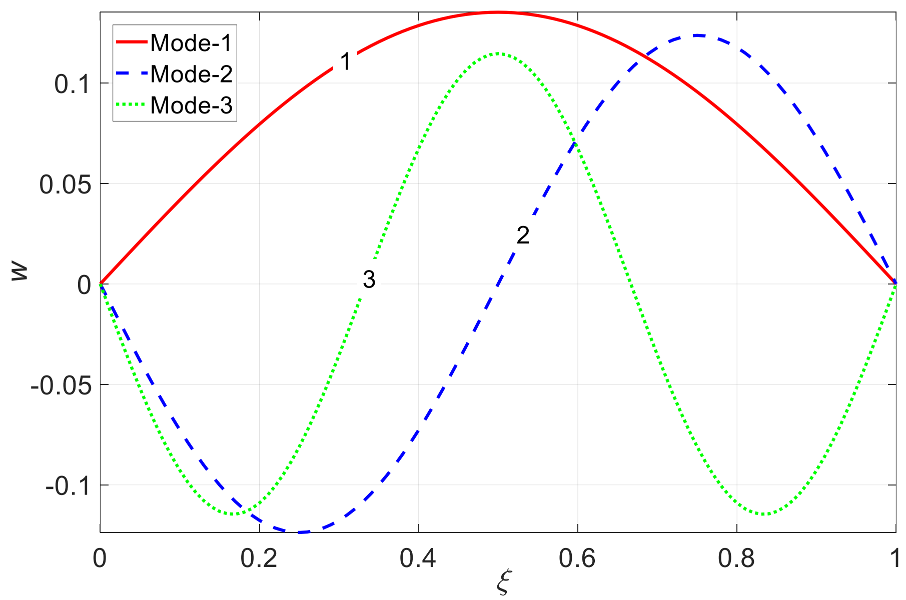

(2) Transverse vibration mode

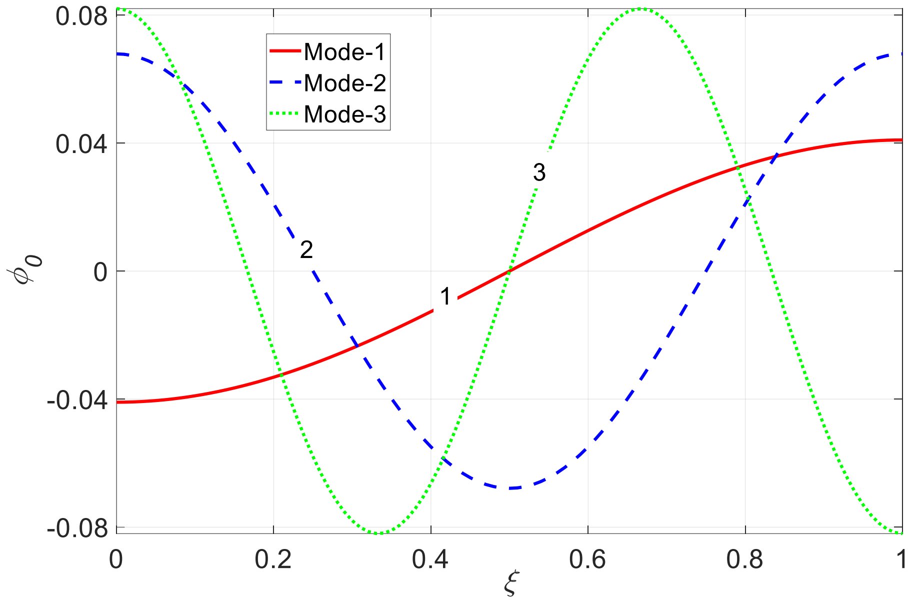

(3) Rotation vibration mode

Fig.6 The mode shape of T1-P-P along *u*, *w* and ϕ_0 directions

4. Nondeterministic analysis of FG porous beams with interval material uncertainties

4.1.Surrogate modelling

As state in the introduction, due to the manufacturing techniques and the inherent complexity in fabrication process, the material physical properties would not be certain values, especially Young's modulus, mass density and porosity coefficient. Furthermore, the uncertainties in material properties cause the uncertainties of mass and stiffness matrices, which will eventually lead to the uncontrollable structural responses.

The traditional nondeterministic analysis based on analytical-numerical method is computationally expensive and inefficient, especially for high-dimensional variables. The relationship between input and output cannot be directly obtained. Under these circumstances, a surrogate modelling for the nondeterministic analysis of FG porous beams with interval material uncertainties is established. Based on this model, the outcome of interest is represented by a function of uncertainty variables and then optimization and sensitivity analysis can be directly applied in this performance function. For example, in 2D system, the response surface can be obtained from the input of a series of α_1 and α_2, as shown in Fig.7. Then surrogate modelling is built to represent the relationship of outputs and inputs.

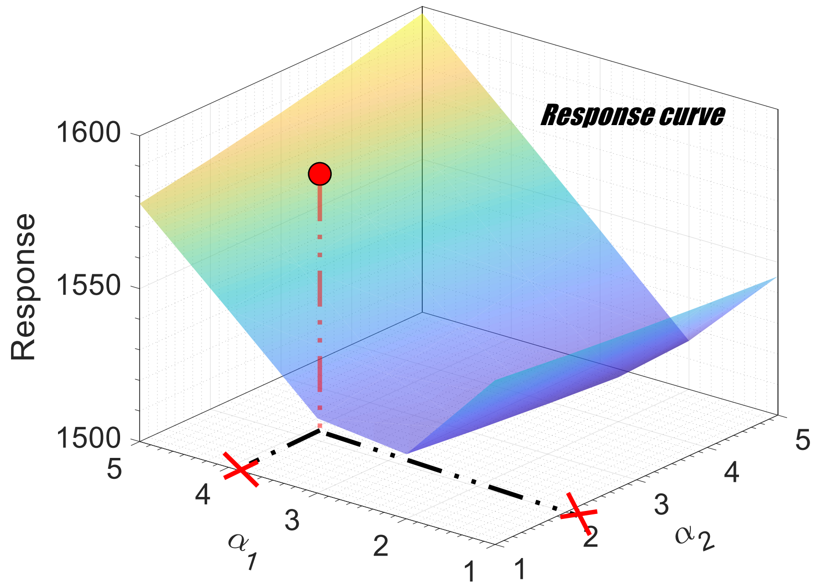

Fig.7 Response curve of a 2D model

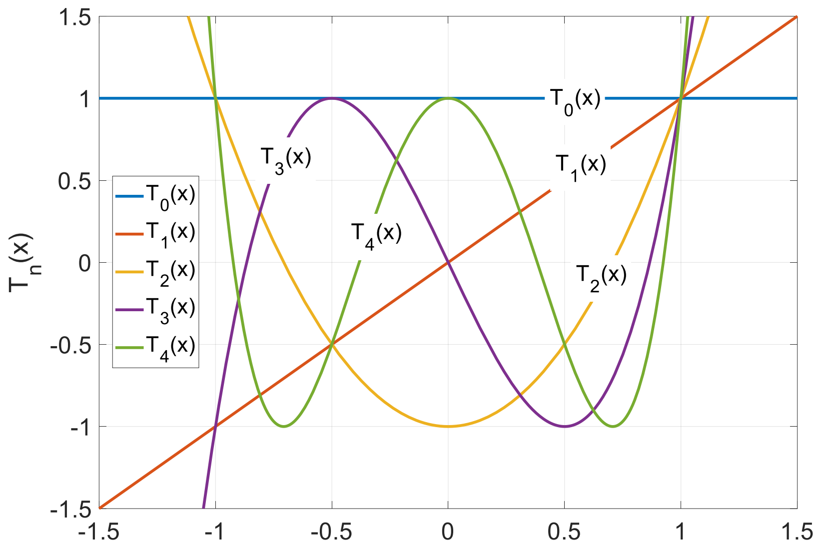

Fig.8 The free five Chebyshev polynomials

In this study, the Chebyshev surrogate model is utilized to conduct the interval analysis of dynamic responses of FG porous beams. According to the definition, the Chebyshev polynomials of the first kind are given as

$$C_n(x) = \cos(n \arccos x) \qquad x \in [-1,1] \tag{25}$$

By introducing a series of degree n into Eq.(25), the recursion formula of Chebyshev polynomials can obtain

$$C(n,x) = 2xC(n-1,x) - C(n-2,x) \tag{26}$$

Based on Eq.(26), the plot of the first five Chebyshev polynomial is shown in Fig.8. Chebyshev polynomials are orthogonal on the interval [-1,1] and corresponding weight function is

$$w(x) = \frac{1}{\sqrt{1-x^2}} \tag{27}$$

For one dimensional system, $f(x)$ can be approximated by the Chebyshev series $g_n(x)$ as follows

$$f(x) \approx g_n(x) = \frac{1}{2} f_0 + \sum_{k=1}^{n} f_k C_k(x) \tag{28}$$

where f_k are the coefficients of Chebyshev expansion and can be obtained by

$$f_k = \frac{2}{\pi}\int_{-1}^{1} \frac{f(x)C_k(x)}{\sqrt{1-x^2}} dx = \frac{2}{m}\sum_{j=1}^{m} f(\cos\theta_j)\cos k\theta_j \tag{29}$$

where m denotes the order of numerical integral formula. To guarantee the best approximation of the continuous function and decrease the imperative error, the order of m should be large than n+1[43]. The interpolation points x_j are the zeros of Chebyshev polynomials for degree m, which can be expressed as

$$x_j = \cos\theta_j = \cos(\frac{2j-1}{2m}\pi),\ j = 1, 2, ..., m \tag{30}$$

In order to show advantages of Chebyshev surrogate model, a simple function f(x) defined as below

$$f(x) = \frac{1}{1+50x^2} \tag{31}$$

The Chebyshev interpolation is compared with the following popular interpolations, such as equally spaced interpolation, Legendre-Gauss interpolation, Legendre-Gauss interpolation and Legendre-Gauss-Lobatto interpolation, as depicted in Fig.8. As can be seen, although the equally spaced interpolation matches very well with exact solution in the central areas, the Rung’s phenomenon is severe on the two boundary conditions. For other interpolations, there is no Rung’s phenomenon, while when we zoom in the peak areas, the following conclusion can be made: Chebyshev surrogate model can minimize the problem of Runge's phenomenon and provides the best approximation to a continuous function with a limited number of interpolation points.

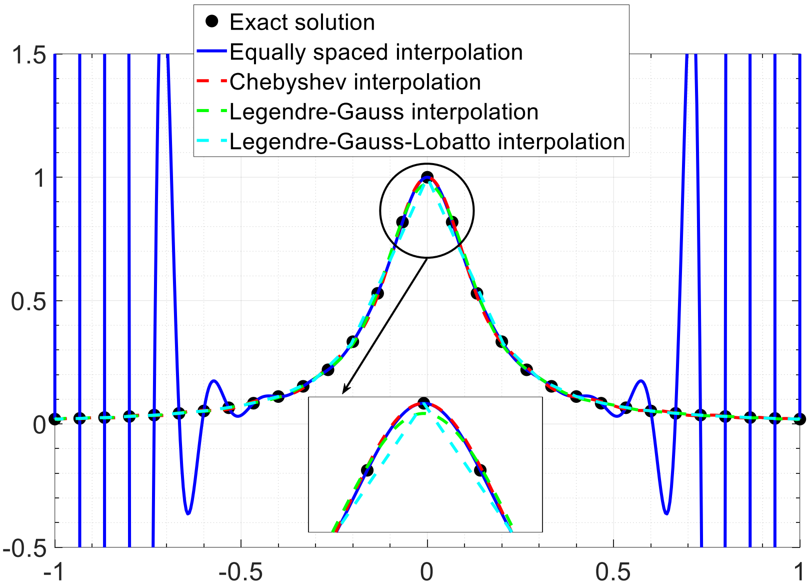

Fig.9 The comparison of different interpolation methods

For higher dimensional issues, the Chebyshev polynomials can be obtained by using the tensor product of each one-dimensional polynomial. For example:

$$C_{n_1,n_2,\ldots,n_k}(x_1,x_2,\ldots,x_k)=C_{n_1}(x_1)C_{n_2}(x_2)\ldots C_{n_k}(x_k),\ x_i\in[-1,1],(i=1,2,\ldots,k) \tag{32}$$

Then the continuous function $f(\mathbf{x})$ on $[\underline{\mathbf{x}},\overline{\mathbf{x}}]$ can be approximated as

$$f(\mathbf{x})\approx g(\mathbf{x})=\sum_{i_1=0}^{n}\cdots\sum_{i_k=0}^{n}\left(\frac{1}{2}\right)^{\chi}f_{i_1,\ldots,i_k}C_{i_1,\ldots,i_k}\left(2\frac{\mathbf{x}-\underline{\mathbf{x}}}{\overline{\mathbf{x}}-\underline{\mathbf{x}}}-1\right) \tag{33}$$

where $\mathbf{x}$, $\overline{\mathbf{x}}$ and $\underline{\mathbf{x}}$ are the matrix of interval variables, the upper bounds of different variables and the lower bounds of the interval variables, which can be expressed as $\mathbf{x}=[x_1,\ldots,x_k]$, $\overline{\mathbf{x}}=[\overline{x}_1,\ldots,\overline{x}_k]$ and $\underline{\mathbf{x}}=[\underline{x}_1,\ldots,\underline{x}_k]$, respectively. χ represents the total number of zeros that exists in the subscripts $i_1,\ldots,i_k$. $C_{i_1,\ldots,i_k}$ is the k-dimensional Chebyshev polynomials and can be calculated from Eq.(32). And the coefficients of higher-dimensional polynomials in each dimension can be determined by

$$\begin{aligned}f_{i_1,\ldots,i_k}&=\left(\frac{2}{\pi}\right)^{k}\int_{-1}^{1}\cdots\int_{-1}^{1}\frac{f(\mathbf{x})C_{i_1,\ldots,i_k}(\mathbf{x})}{\sqrt{1-x_1^2}\cdots\sqrt{1-x_k^2}}dx_1\cdots dx_k\\&\approx\left(\frac{2}{m}\right)^{k}\sum_{j_1=1}^{m}\cdots\sum_{j_k=1}^{m}f(\cos\theta_{j_1},\ldots,\cos\theta_{j_k})\cos i_1\theta_{j_1},\ldots,\cos i_k\theta_{j_k}\end{aligned} \tag{34}$$

where i is the number of interval variables and m denotes the order of numerical integral formula. And the interpolation points $\cos\theta_j$ in each dimension are the zeros of Chebyshev polynomials for degree m_k and reformulated from Eq.(30)

$$\cos\theta_{j_k} = \cos\left(\frac{2j_k - 1}{2m_k}\pi\right),\ j_k = 1, 2, ..., m_k \tag{35}$$

Once the deterministic analysis from DSC is obtained, the proposed non-inclusive CSM can be easily implemented to capture the upper and lower bounds of the structural responses.

4.2.The verification and accuracy of nondeterministic analysis

In this subsection, the results of dynamic characteristics analysis of FG porous beams are proposed based on hybrid CSM-DSC by interval analysis. The uncertain porosity coefficient (**N_0^I**), Young's modulus (**E^I**, Pa) and mass density (**ρ^I**, kg/m^3) with interval ranges adopted in this study, which is defined as

$$\begin{aligned} \boldsymbol{N}_0^I &= N_0^{mean}(1 \pm \beta_1) \\ \boldsymbol{E}_0^I &= E_0^{mean}(1 \pm \beta_2) \\ \rho_0^I &= \rho_0^{mean}(1 \pm \beta_3) \end{aligned} \tag{36}$$

where $\boldsymbol{N_0^I}$, $\mathbf{E^I}$ and $\boldsymbol{\rho^I}$ are the interval range of porosity coefficient, Young's modulus and mass density; N_0^{mean}, E_0^{mean} and ρ_0^{mean} are the mean values of these values, like E_0^{mean}=200GPa, ρ_0^{mean}=7850kg/m^3, N_0^{mean}=0.8; β_1, β_2 and β_3 are the uncertainty degrees of the variables. If we define β_1=β_2=β_3=0.2, the interpolation points of uncertain variables can be expressed as

$$\begin{aligned} \boldsymbol{N}_0^I &\in \boldsymbol{\varphi}_{N_0} := \left\{ \boldsymbol{N_0} \in \Re^{n_1} \,\middle|\, 0.64 \le N_{0,k_1} \le 0.96, k_1 = 1, 2, ..., n_1 \right\} \\ \boldsymbol{E}^I &\in \boldsymbol{\varphi}_E := \left\{ \boldsymbol{E} \in \Re^{n_2} \,\middle|\, 160\times10^9 \le E_{k_2} \le 240\times10^9, k_2 = 1, 2, ..., n_2 \right\} \\ \rho^I &\in \boldsymbol{\varphi}_\rho := \left\{ \rho \in \Re^{n_3} \,\middle|\, 6280 \le \rho_{k_3} \le 9420, k_3 = 1, 2, ..., n_3 \right\} \end{aligned} \tag{37}$$

where k_1, k_2 and k_3 are the dimensional number in Chebyshev polynomials while n_1, n_2 and n_3 denote the interpolation points in each dimension, respectively.

To demonstrate the effectiveness and efficiency of the proposed method for nondeterministic dynamic characteristics of FG porous beams, four different boundary conditions are considered, such as pinned-pinned (P-P), clamped-clamped (C-C), clamped-pinned (C-P), clamped-free (C-F). Firstly, the proposed nondeterministic method is validated with QMCS method, which adopts low-discrepancy Sobol sequence by skipping the first 1000 values and retaining every 101st points for generating all the interval samplings. Table.4 shows the results of proposed method and QMCS method for different boundary conditions. For QMCS, 10,000 simulations have been implemented for interval analysis. Here the results of upper bounds of natural frequencies are just considered as example to show the accuracy and efficiency of the present method. As shown in this table, the present method matches very good with the traditional sampling method QMCS for the cases. With the same accuracy, the present method greatly improves the computing speed.

Table.4 Comparison of the upper bounds of natural frequencies and computational time of various boundary conditions for proposed method and QMCS method (T1)

Type	P-P		C-C		C-P		C-F	
	Natural frequency	Computational time	Natural frequency	Computational time	Natural frequency	Computational time	Natural frequency	Computational time
Proposed method	1707.2254	115.9 s	3550.979	118.7 s	2570.848	101.9 s	617.6347	102.7 s
QMCS	1707.2223	0.93 h	3550.973	0.92 h	2570.843	0.94 h	617.6335	0.93 h

Table.5 The first ten frequencies of proposed method, deterministic results and QMCS method with P-P boundary condition for T1

Mode Number	Upper bounds			Deterministic results	Lower bounds		
	Proposed	QMCS	Relative error(%)		Proposed	QMCS	Relative error(%)
1	1707.23	1707.22	1.81E-06	1556.75	1513.34	1513.35	4.89E-06
2	6320.18	6320.17	1.86E-06	5816.73	5687.76	5687.79	4.88E-06
3	12825.39	12825.36	1.91E-06	11925.18	11740.32	11740.38	4.86E-06
4	14995.36	14995.44	-4.84E-06	14635.25	14587.22	14587.15	-4.49E-06
5	20380.55	20380.51	1.94E-06	19121.66	18943.91	18944.01	4.86E-06
6	28469.34	28469.28	1.95E-06	26907.22	26785.84	26785.74	-3.72E-06
7	29990.73	29990.87	-4.84E-06	29270.50	29174.44	29174.31	-4.49E-06
8	36808.95	36808.87	1.95E-06	34991.93	34923.80	34923.94	4.18E-06
9	44905.71	44907.03	-2.94E-05	43214.75	43183.19	43185.05	4.31E-05
10	45251.83	45250.33	3.30E-05	43905.75	43761.89	43761.46	-9.87E-06

Table.6 The first ten frequencies of proposed method, deterministic results and QMCS method with C-C boundary condition for T1

Mode Number	Upper bounds			Deterministic results	Lower bounds		
	Proposed	QMCS	Relative error(%)		Proposed	QMCS	Relative error(%)
1	3550.98	3550.97	1.82E-06	3271.69	3202.88	3202.90	4.88E-06
2	8719.97	8719.95	1.87E-06	8127.61	8018.87	8018.91	4.87E-06
3	15031.01	15030.47	3.59E-05	14307.36	14204.85	14205.04	1.35E-05
4	15212.35	15212.83	-3.18E-05	14695.34	14647.21	14647.05	-1.09E-05
5	22453.49	22453.44	1.93E-06	21262.56	21191.89	21191.90	6.71E-07
6	30058.74	30060.95	-7.35E-05	28705.08	28663.55	28663.62	2.50E-06
7	30159.46	30157.13	7.71E-05	29390.69	29294.14	29294.10	-1.34E-06
8	38142.01	38141.94	1.95E-06	36451.48	36431.91	36432.04	3.42E-06

9	45089.74	45091.45	-3.79E-05	44086.05	43941.75	43941.17	-1.31E-05
10	46295.48	46293.60	4.07E-05	44385.04	44377.57	44379.34	3.98E-05

Table.7 The first ten frequencies of proposed method, deterministic results and QMCS method with C-P boundary condition for T1

Mode Number	Upper bounds			Deterministic results	Lower bounds		
	Proposed	QMCS	Relative error(%)		Proposed	QMCS	Relative error(%)
1	2570.85	2570.84	1.82E-06	2356.30	2298.46	2298.47	4.88E-06
2	7546.42	7546.41	1.87E-06	6991.59	6868.48	6868.51	4.87E-06
3	14057.80	14057.77	1.90E-06	13153.67	13009.96	13010.02	4.86E-06
4	14995.36	14995.44	-4.84E-06	14635.25	14587.22	14587.15	-4.49E-06
5	21435.39	21435.35	1.93E-06	20216.06	20103.90	20103.81	-4.76E-06
6	29294.89	29294.84	1.94E-06	27797.96	27727.01	27727.10	3.15E-06
7	29990.73	29990.87	-4.84E-06	29270.50	29174.44	29174.31	-4.49E-06
8	37419.34	37419.26	1.95E-06	35677.08	35639.97	35640.11	4.07E-06
9	44905.66	44907.03	-3.05E-05	43720.57	43702.50	43706.51	9.19E-05
10	45683.01	45681.47	3.38E-05	43905.75	43821.07	43793.58	-6.28E-04

Table.8 The first ten frequencies of proposed method, deterministic results and QMCS method with C-F boundary condition for T1

Mode Number	Upper bounds			Deterministic results	Lower bounds		
	Proposed	QMCS	Relative error(%)		Proposed	QMCS	Relative error(%)
1	617.63	617.63	1.80E-06	562.05	545.70	545.70	4.89E-06
2	3583.74	3583.73	1.86E-06	3293.10	3216.63	3216.65	4.88E-06
3	7497.68	7497.72	-4.84E-06	7317.62	7293.61	7293.58	-4.49E-06
4	9087.76	9087.74	1.92E-06	8436.76	8296.18	8296.22	4.86E-06
5	15900.70	15900.67	1.96E-06	14902.97	14749.97	14750.04	4.85E-06
6	22452.92	22453.52	-2.66E-05	21952.87	21881.00	21880.73	-1.23E-05
7	23479.96	23479.28	2.92E-05	22173.11	22109.08	22091.47	-7.97E-04
8	31462.51	31462.44	2.00E-06	29892.04	29820.60	29820.70	3.47E-06
9	37488.41	37488.59	-4.84E-06	36588.12	36468.05	36467.88	-4.49E-06
10	39646.61	39646.53	2.02E-06	37852.63	37817.53	37817.68	3.99E-06

Table 5-8 show the first ten frequencies of proposed method, deterministic results and QMCS method for various boundary conditions with T1 distribution pattern. As can be seen, the proposed method has a good agreement with the QMCS for both upper bounds and lower bounds. The deterministic results are well embraced by the nondeterministic method. Due to the material uncertainties involving in the system, the original dimensionless definition in Eq.(17) no longer apply.

If we draw these tables into figures, as depicted in Fig.10, three findings can be witnessed: Firstly, the proposed method has a good agreement with QMCS for both lower and upper bounds; Secondly, the influence of uncertainties is not linear because the deterministic results lean to the lower bounds. Lately, the curve of frequency increase is not linear and there is some zig-zag phenomenon. This is because, in general, the researchers just considered transverse vibration in the systems. While in present study, 3D vibration is included, as shown in Fig.6. For example, for P-P boundary condition, the frequency of mode 4, 7 and 9 is due to longitudinal vibration. The turning points are marked in green circle in the figures. We also found that for different FG porous types and boundary conditions, the mode shape jump phenomena might be different.

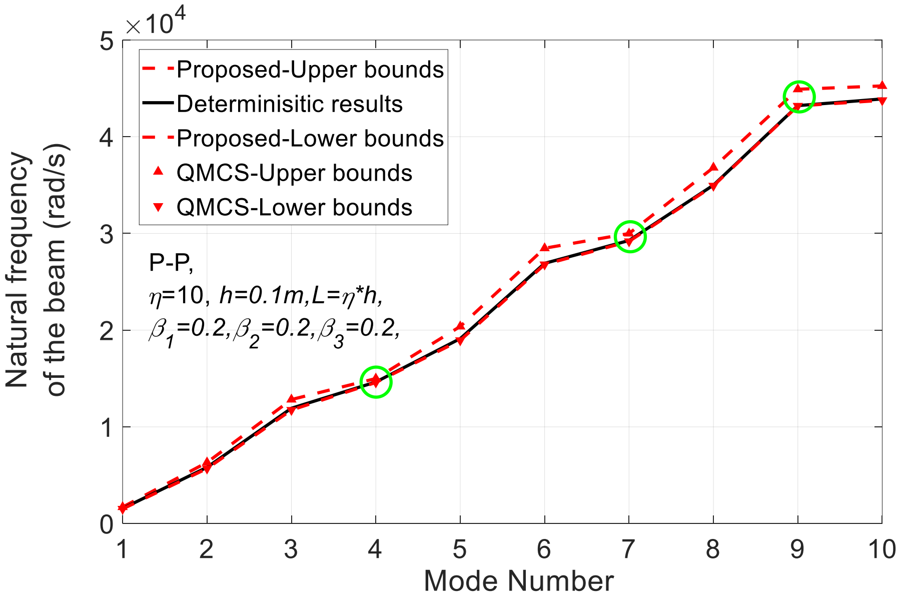

(a) P-P

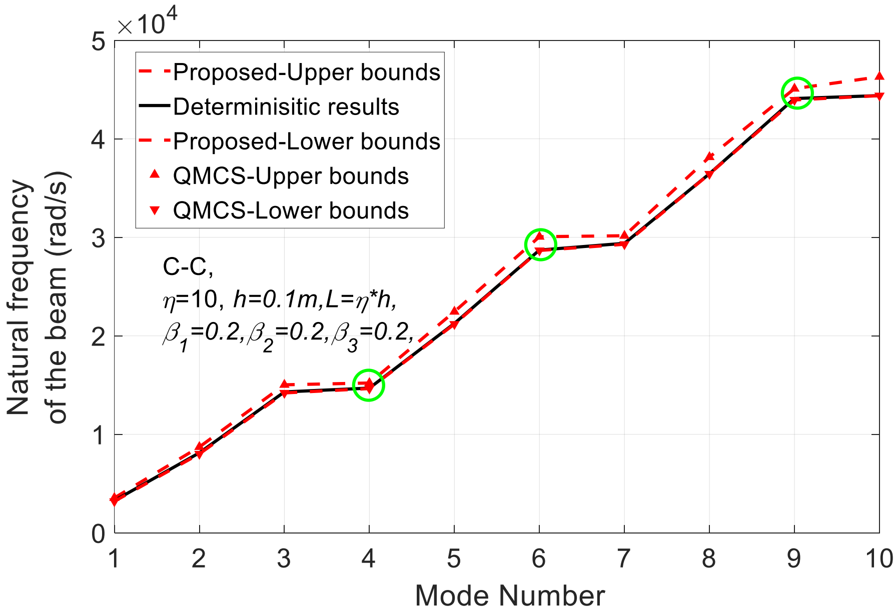

(b) P-P

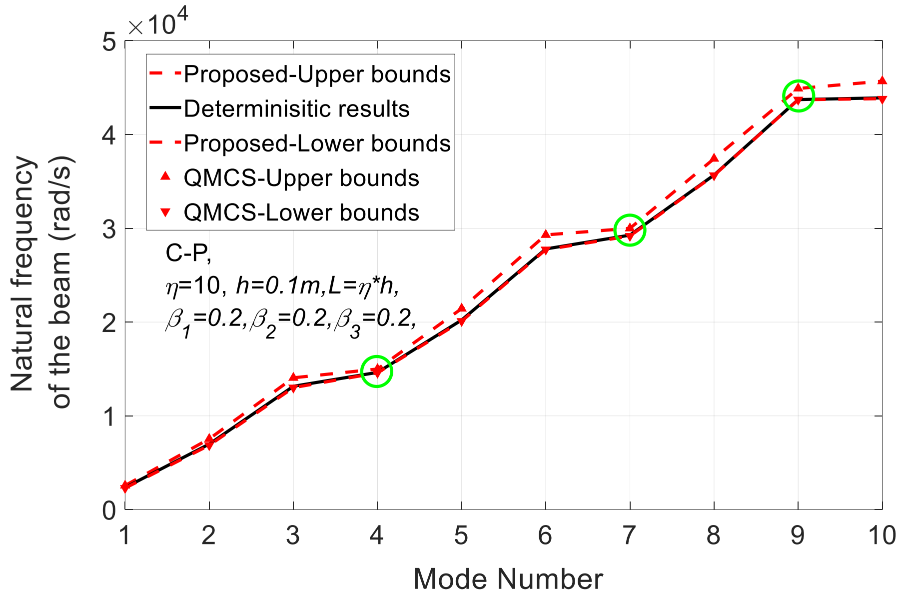

(c) C-P

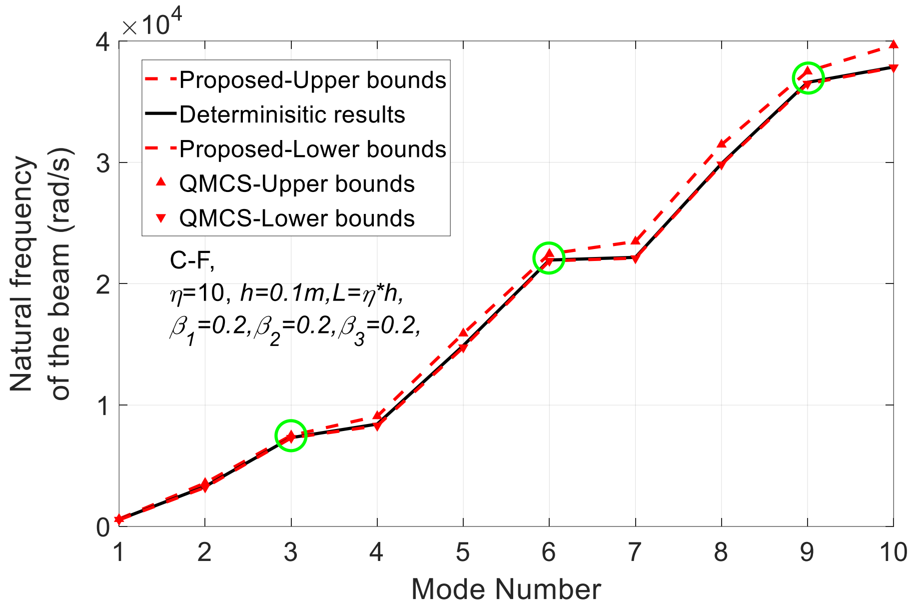

(d) C-F

Fig.10 The upper bounds, deterministic results and low bounds of natural frequency obtained from proposed methods, deterministic analysis and QMCS for different mode numbers and boundary conditions

Then, the uncertain mode shape is also examined by the QMCS method in Fig.11. The first mode shapes of different boundary conditions are investigated. As clearly indicated in Fig.11, the mode shapes predicted by the proposed method are in good agreement with QMCS sampling. The results of QMCS sampling are well embraced by areas that form between the upper bounds and lower bounds of the proposed method.

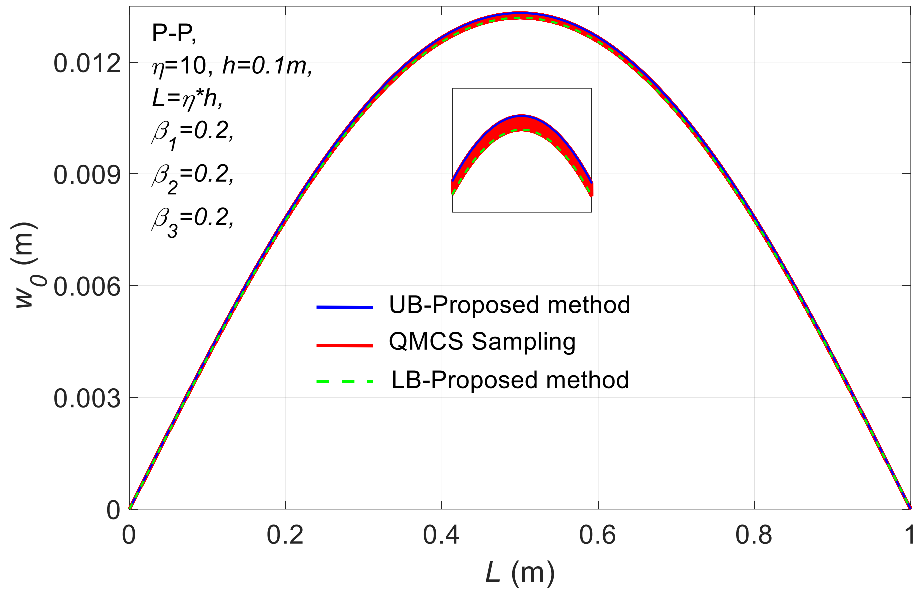

(a) P-P

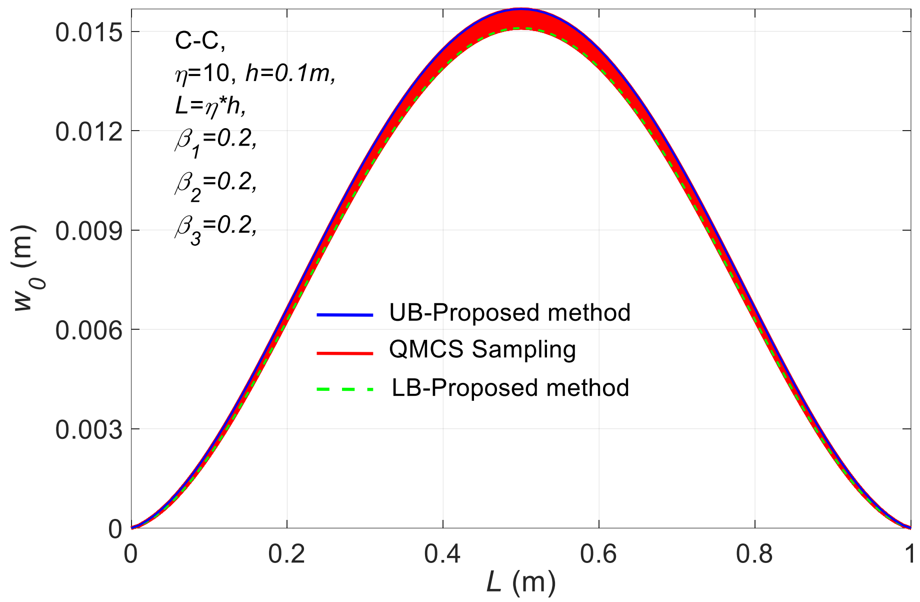

(b) C-C

4.3. The influence of distribution patterns, boundary conditions, aspect ratios and midpoint of porosity coefficients on bounds of natural frequencies

From last section, the validity and accuracy of the proposed method are comprehensively investigated by comparing the results of frequencies and the mode shapes of different boundary conditions with QMCS method and deterministic analysis. In this section, the influence of distribution patterns, boundary conditions, aspect ratios and midpoint of porosity coefficients on the bounds of natural frequencies are studied.

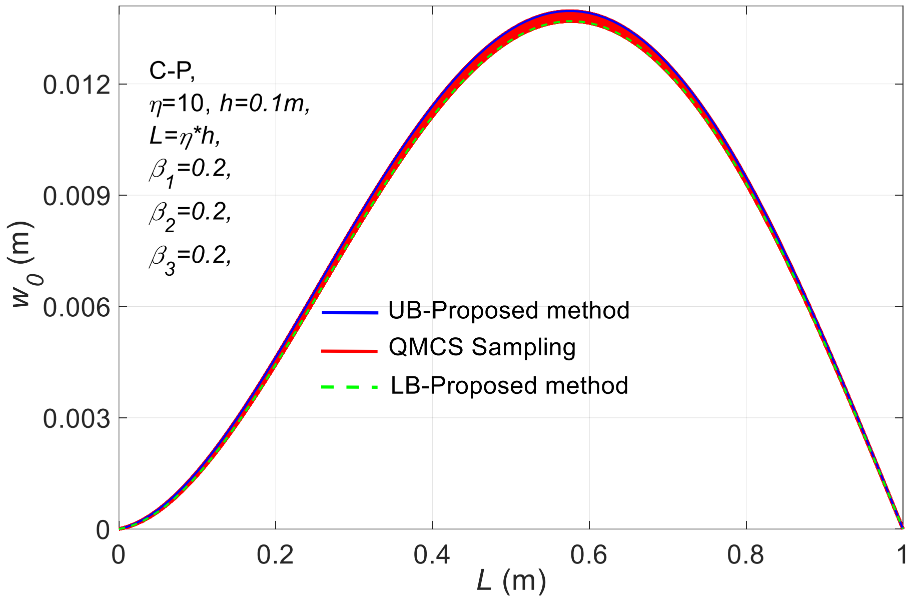

(c) C-P

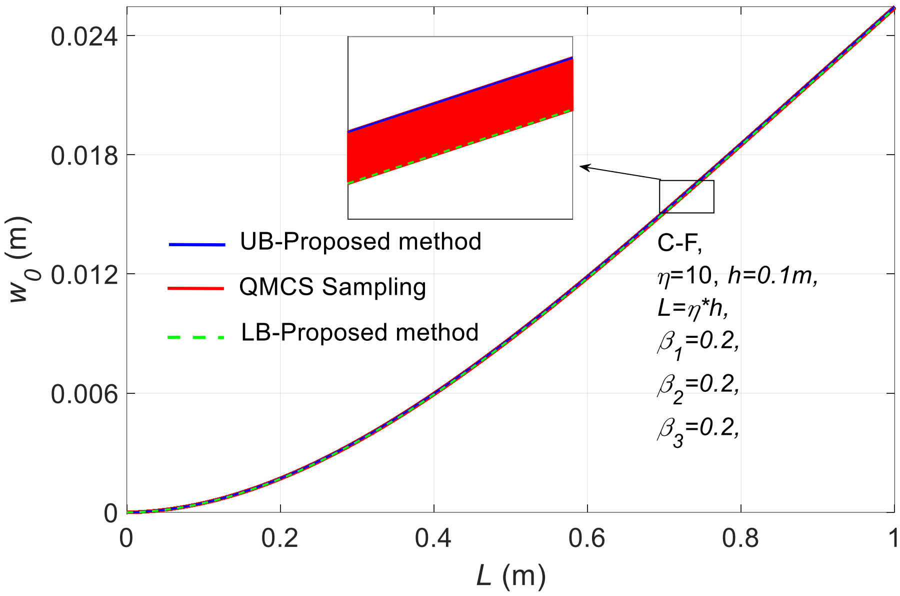

(d) C-F

Fig.11 The first mode shape of the upper bounds, low bounds and results of QMCS with 10,000 samplings for different boundary conditions of T1

Fig.12 depicts the change of midpoint of porosity coefficients on the bounds of different distribution patterns, such as N_0^{mean} =0.2, 0.4, 0.6 and 0.8. E_0^{mean} =200GPa, ρ_0^{mean} =7850kg/m^3 are the same as before. β_1=β_2=β_3 =0.1, which means 10% uncertainty degree for all variables. P-P boundary condition is considered as an example here. With the increase of the midpoint of porosity coefficients, the width between upper and lower bounds magnifies, while T2 and T4 are sensitive to the uncertainty degrees.

Then the influence of uncertainty variables on *L/h* is plot in Fig.13. N_0^{mean}=0.6 and other parameters remain unchanged. Four different *L/h* are considered, like 20, 40, 60 and 80. As can be seen, the *L/h* has little effect on the frequency bounds of different distribution patterns. Fig.14 demonstrates the uncertainty bounds for various distribution patterns and boundary conditions. Clearly, T1 has the largest natural frequency, and the boundary conditions of C-C and C-P are sensitive to the uncertain variables.

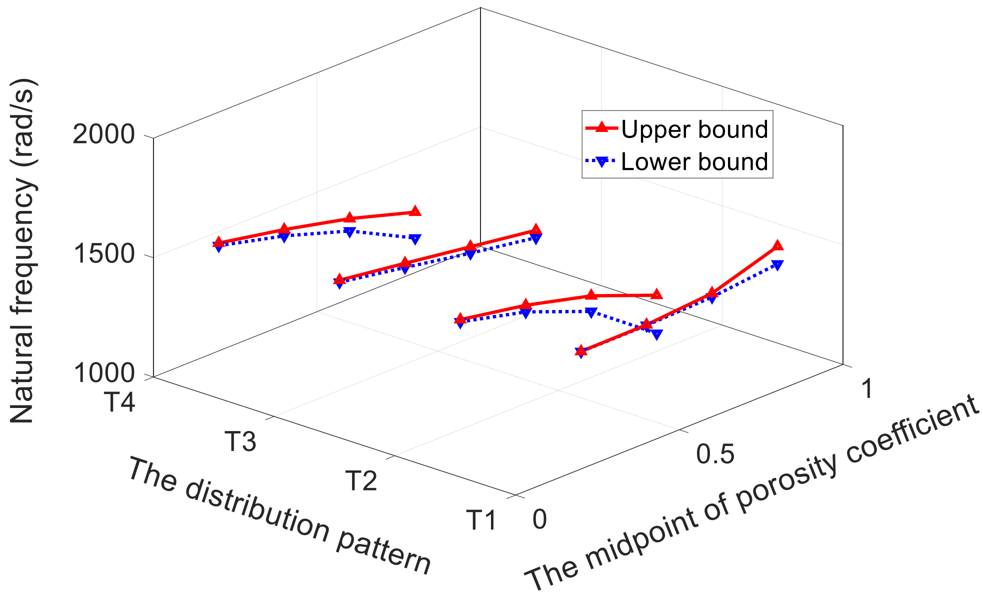

Fig.12 The uncertain bounds for different distribution patterns and midpoint of porosity coefficients

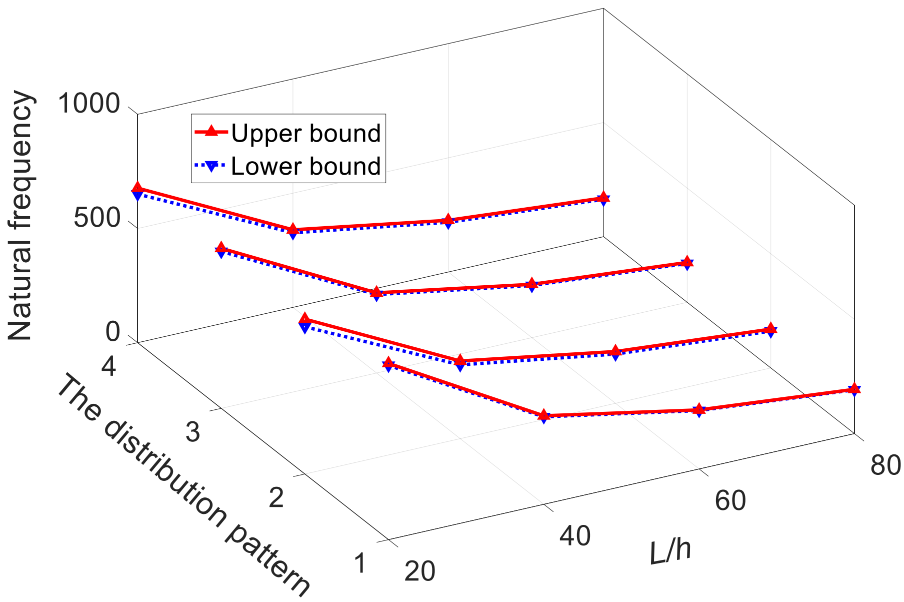

Fig.13 The uncertainty bounds for different distribution patterns and *L/h*

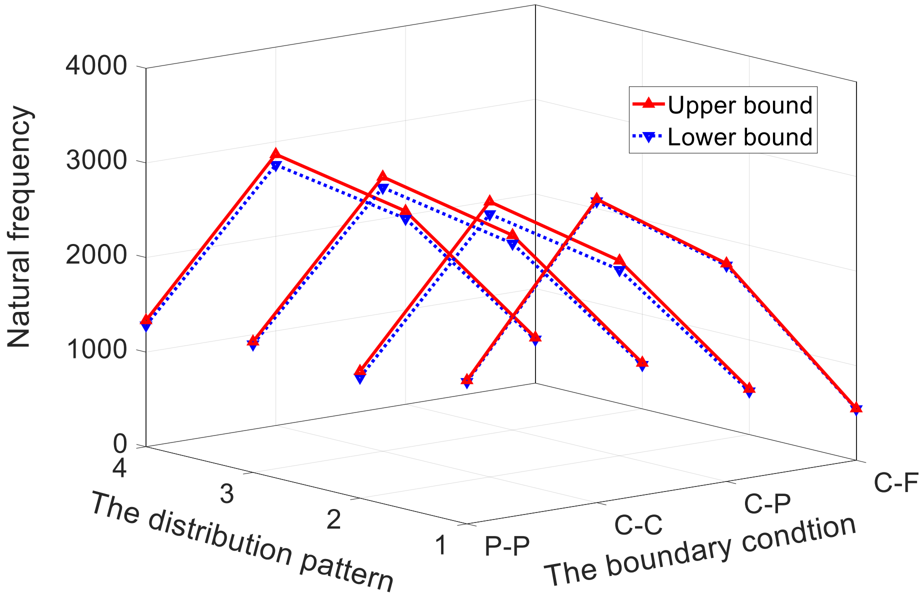

Fig.14 The uncertainty bounds for different distribution patterns and boundary conditions

4.4.The influence of uncertainty of interval variables on the bounds of natural frequencies

To further investigate the influence of fluctuations of uncertain porosity coefficients, Young's modulus and mass density on frequencies of FG porous beams, the combination of different uncertain degrees of the three pivotal material properties, including 4%, 8%,12%,16% and 20% of uncertain degrees of Young's modulus, porosity coefficient and mass density, are studied, respectively. By utilizing the proposed method, the response surfaces of natural frequency for different change ranges of Young's modulus, mass density and porosity coefficient of T1 with P-P boundary condition are shown in Fig.15-Fig.17. N_0^{mean} =0.6, E_0^{mean} =200GPa and ρ_0^{mean} =7850kg/m^3.

Fig.15 depicts the bounds of frequencies for change ranges of Young's modulus and porosity coefficient. In this case, β_1=0.1, and β_2= β_3=0.04,0.08,0.12,0.16 and 0.2, respectively. It is clearly that uncertainty degree of natural frequency was proportional to change range of porosity coefficient. While for Young's modulus, the natural frequencies firstly decrease and then increase when the uncertainty degree of β_2 increases from 4% to 20%. The upper bounds and lower bounds are anti-symmetry for different natural frequencies.

The bounds of frequencies for various change ranges of mass density and porosity coefficient is shown in Fig.16. In this case, β_2=0.1, and β_1= β_3=0.04,0.08,0.12,0.16 and 0.2, respectively. From the results, when the uncertainty degree of mass density at 4%, the natural frequencies increase with the increase of change range of porosity coefficient. However, the natural frequencies linearly decrease when β_3 equals 20%. The one DOF (degree-of-freedom) system is taken as an example to explain this phenomenon. This following equation gives the relationship between frequency, stiffness and mass:

$$f = \frac{1}{2\pi}\sqrt{\frac{K}{M}}; \omega = \sqrt{\frac{K}{M}} \tag{38}$$

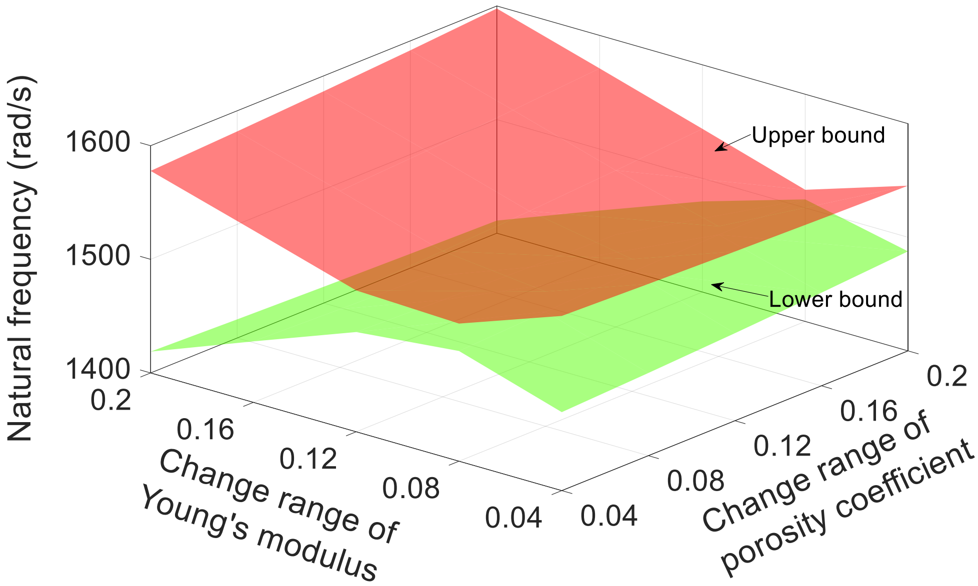

Fig.15 Bounds of frequencies for Young's modulus and porosity coefficient with different change ranges

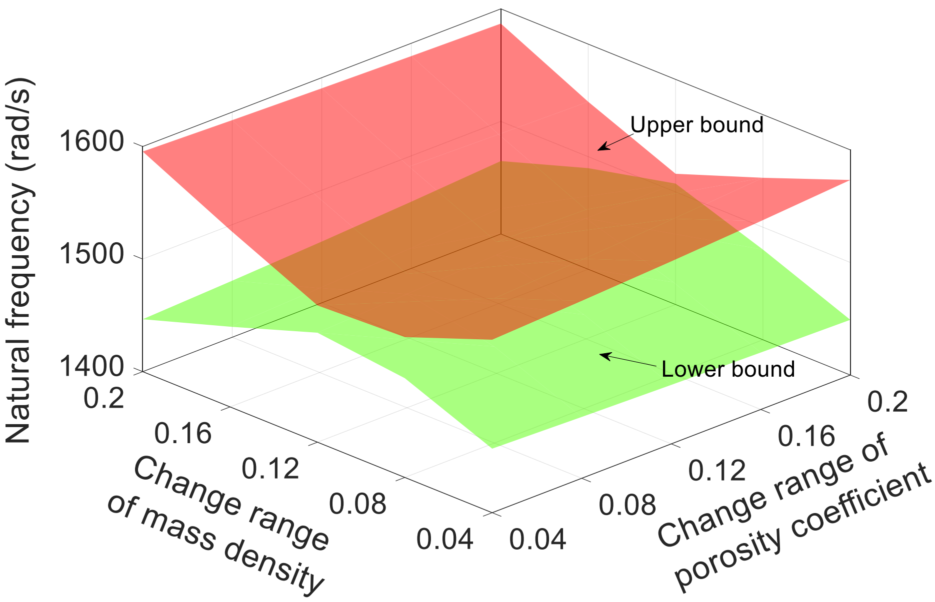

Fig.16 Bounds of frequencies for mass density and porosity coefficient with different change ranges

For 1D system, the increasing mass will lead to the decrease of frequencies if the stiffness is a constant. While in present study, the FG porous beam was discrete to a series of nodes, then the stiffness and mass matrices are obtained by using the DSC method. When the change ranges of mass density are small, like 4% in this case, the relationship between stiffness and mass matrices will lead to the increase of natural frequency. Similarly, if the uncertainty degree of mass density become larger, like 20% in this case, the natural frequencies decrease due to wax and wane of the two factors. Such phenomenon is quite clear in Fig.17, which indicts bounds of frequencies due to different uncertainty degrees of mass density and Young's modulus directly. The further explanation is omitted here. From these three figures, we can also conclude that the uncertain of Young's modulus has a significant effect on frequencies, then mass density; while the influence of the uncertain of porosity coefficient is less pronounced.

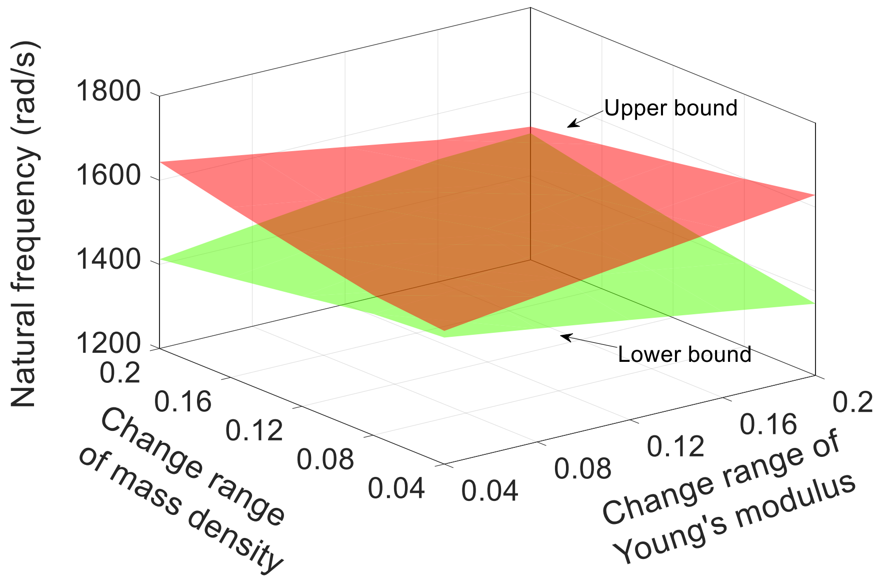

Fig.17 Bounds of frequencies for Young's modulus and mass density with different change ranges

5. Conclusions

This article presents a novel computational approach, named hybrid CSM-DSC method, for nondeterministic dynamic analysis of FG porous beams with material uncertainties. Based on this computational framework, the upper bounds and low bounds of the dynamic responses of FG porous beams with various boundary conditions is obtained by using interval analysis directly. This hybrid method shares the advantages of Chebyshev surrogate model and discrete singular convolution method in both accuracy and effectiveness, which means CSM can dramatically reduce the cost of interval analysis and remain the correctness through the DSC method by the analytical-numerical solutions.

From the two steps examination, deterministic analysis and nondeterministic analysis, the accuracy and validity of the proposed method are justified by comparing the results of other authors, FEM and the QMCS method. Finally, the influence of porosity distribution patterns, porosity coefficient, boundary conditions, aspect ratio on the bounds of frequencies and the influence of material parameters with various uncertainty degrees are comprehensively studied and some of the conclusions can be summarized as follows:

1. T1 possesses the maximum frequencies while T2 is the least one; The differences between T3 and T4 were much less pronounced;
2. The increase of porosity coefficients would lead to the linearly decrease of both mass density and stiffness of the structures while the frequencies not necessarily decrease. For FG porous structures with multiple uncertainties, the responses of the systems are different, even opposite.
3. For different FG porous types and boundary conditions, the mode shape jump phenomena might be different.
4. The uncertain of Young's modulus has a significant effect on dynamic responses, then mass density; while the influence of the uncertain of porosity coefficient is the least.
5. The nondeterministic dynamic characteristics can help design of FG porous structures working dynamical environment, especially for nano/micro-sized devices and systems.

The developed method offers a superior way for dynamic characteristics with insufficient experimental data more fast, efficient and flexible, which provide references for engineers in the design of porous structures.

Acknowledgements

The work described in the present paper is fully funded by a research grant from the Australian Research Council under Discovery Project scheme (DP160101978). The authors are grateful for the financial support.

Declaration of Interests

All authors declare that they do not have any conflict of interest in the work presented in this paper.

References

[1] Daxner T, Rammerstorfer FG, Böhm HJ. Adaptation of density distributions for optimising aluminium foam structures. Mater Sci Technol. 2000;16:935-9.

[2] Nogata F, Takahashi H. Intelligent functionally graded material: bamboo. Compos Eng. 1995;5:743-51.

[3] Chen D, Yang J, Kitipornchai S. Elastic buckling and static bending of shear deformable functionally graded porous beam. Compos Struct. 2015;133:54-61.

[4] Shen H-S, Lin F, Xiang Y. Nonlinear bending and thermal postbuckling of functionally graded graphene-reinforced composite laminated beams resting on elastic foundations. Eng Struct. 2017;140:89-97.

[5] Gao K, Gao W, Wu D, Song C. Nonlinear dynamic characteristics and stability of composite orthotropic plate on elastic foundation under thermal environment. Compos Struct. 2017;168:619-32.

[6] Chen D, Yang J, Kitipornchai S. Free and forced vibrations of shear deformable functionally graded porous beams. Int J Mech Sci. 2016;108:14-22.

[7] Chen D, Yang J, Kitipornchai S. Nonlinear vibration and postbuckling of functionally graded graphene reinforced porous nanocomposite beams. Compos Sci Technol. 2017;142:235-45.

[8] Yang J, Chen D, Kitipornchai S. Buckling and free vibration analyses of functionally graded graphene reinforced porous nanocomposite plates based on Chebyshev-Ritz method. Compos Struct. 2018;193:281-94.

[9] Gao K, Gao W, Wu D, Song C. Nonlinear dynamic stability analysis of Euler–Bernoulli beam–columns with damping effects under thermal environment. Nonlinear Dynamics. 2017;90:2423-44.

[10] Gao K, Gao W, Wu D, Song C. Nonlinear dynamic stability of the orthotropic functionally graded cylindrical shell surrounded by Winkler-Pasternak elastic foundation subjected to a linearly increasing load. Journal of Sound and Vibration. 2018;415:147-68.

[11] Gao K, Gao W, Wu D, Song C. Nonlinear dynamic buckling of the imperfect orthotropic E-FGM circular cylindrical shells subjected to the longitudinal constant velocity. Int J Mech Sci. 2018;138:199-209.

[12] Gao K, Huang Q, Kitipornchai S, Yang J. Nonlinear dynamic buckling of functionally graded porous beams. Mech Adv Mater Struct. 2019:1-12.

[13] Gao K, Gao W, Wu B, Wu D, Song C. Nonlinear primary resonance of functionally graded porous cylindrical shells using the method of multiple scales. Thin-Walled Struct. 2018;125:281-93.

[14] Ziane N, Meftah SA, Ruta G, Tounsi A. Thermal effects on the instabilities of porous FGM box beams. Eng Struct. 2017;134:150-8.

[15] Bartolucci SF, Paras J, Rafiee MA, Rafiee J, Lee S, Kapoor D et al. Graphene–aluminum nanocomposites. MaterSciEng,A. 2011;528:7933-7.

[16] Duarte I, Ventura E, Olhero S, Ferreira JM. An effective approach to reinforced closed-cell Al-alloy foams with multiwalled carbon nanotubes. Carbon. 2015;95:589-600.

[17] Rashad M, Pan F, Tang A, Asif M. Effect of graphene nanoplatelets addition on mechanical properties of pure aluminum using a semi-powder method. Pro Nat Sci Mater. 2014;24:101-8.

[18] Feng C, Kitipornchai S, Yang J. Nonlinear free vibration of functionally graded polymer composite beams reinforced with graphene nanoplatelets (GPLs). Eng Struct. 2017;140:110-9.

[19] Xu Z, Huang Q. Vibro-acoustic analysis of functionally graded graphene-reinforced nanocomposite laminated plates under thermal-mechanical loads. Eng Struct. 2019;186:345-55.

[20] Huang Y, Yang Z, Liu A, Fu J. Nonlinear buckling analysis of functionally graded graphene reinforced composite shallow arches with elastic rotational constraints under uniform radial load. Materials. 2018;11:910.

[21] Yang Z, Huang Y, Liu A, Fu J, Wu D. Nonlinear in-plane buckling of fixed shallow functionally graded graphene reinforced composite arches subjected to mechanical and thermal loading. Appl Math Model. 2019;70:315-27.

[22] Kitipornchai S, Chen D, Yang J. Free vibration and elastic buckling of functionally graded porous beams reinforced by graphene platelets. Mater Design. 2017;116:656-65.

[23] Gao K, Gao W, Chen D, Yang J. Nonlinear free vibration of functionally graded graphene platelets reinforced porous nanocomposite plates resting on elastic foundation. Compos Struct. 2018;204:831-46.

[24] García-Macías E, Castro-Triguero R, Friswell MI, Adhikari S, Sáez A. Metamodel-based approach for stochastic free vibration analysis of functionally graded carbon nanotube reinforced plates. Compos Struct. 2016;152:183-98.

[25] Dey S, Mukhopadhyay T, Adhikari S. Stochastic free vibration analysis of angle-ply composite plates–A RS-HDMR approach. Compos Struct. 2015;122:526-36.

[26] Gao K, Gao W, Wu B, Song C. Nondeterministic dynamic stability assessment of Euler–Bernoulli beams using Chebyshev surrogate model. Appl Math Model. 2019;66:1-25.
[27] Wu D, Gao W, Gao K, Tin-Loi F. Robust safety assessment of functionally graded structures with interval uncertainties. Compos Struct. 2017;180:664-85.
[28] Wu D, Liu A, Huang Y, Huang Y, Pi Y, Gao W. Mathematical programming approach for uncertain linear elastic analysis of functionally graded porous structures with interval parameters. Compos Part B-Eng. 2018;152:282-91.
[29] Ma J, Du W, Gao W, Wriggers P, Xue X. Multiscale finite element analysis of uncertain-but-bounded heterogeneous materials at finite deformation. Finite Elem Anal Des. 2018;149:15-31.
[30] Wu D, Liu A, Huang Y, Huang Y, Pi Y, Gao W. Dynamic analysis of functionally graded porous structures through finite element analysis. Eng Struct. 2018;165:287-301.
[31] Wang Y, Wu D. Free vibration of functionally graded porous cylindrical shell using a sinusoidal shear deformation theory. Aerospace Science and Technology. 2017;66:83-91.
[32] Jabbari M, Mojahedin A, Haghi M. Buckling analysis of thin circular FG plates made of saturated porous-soft ferromagnetic materials in transverse magnetic field. Thin-Walled Struct. 2014;85:50-6.
[33] Jabbari M, Mojahedin A, Joubaneh EF. Thermal Buckling Analysis of Circular Plates Made of Piezoelectric and Saturated Porous Functionally Graded Material Layers. J Eng Mech. 2014;141:04014148.
[34] Mojahedin A, Joubaneh EF, Jabbari M. Thermal and mechanical stability of a circular porous plate with piezoelectric actuators. Acta Mech. 2014;225:3437-52.
[35] Mojahedin A, Jabbari M, Khorshidvand A, Eslami M. Buckling analysis of functionally graded circular plates made of saturated porous materials based on higher order shear deformation theory. Thin-Walled Structures. 2016;99:83-90.
[36] Gibson LJ, Ashby MF. The mechanics of three-dimensional cellular materials. Proceedings of the Royal Society of London A: Mathematical, Physical and Engineering Sciences: The Royal Society; 1982. p. 43-59.
[37] Wang X, Yuan Z. Comparison of FDSPM and DSC algorithms for free vibration analysis. Appl Math Lett. 2019.
[38] Wang X. Novel discrete singular convolution for high-frequency vibration analysis of structural elements. AIAA Journal. 2017:4364-75.

[39] Wei G, Zhao Y, Xiang Y. Discrete singular convolution and its application to the analysis of plates with internal supports. Part 1: Theory and algorithm. Int J Numer Meth Eng. 2002;55:913-46.
[40] Qian L, Wei G. A note on regularized Shannon's sampling formulae. arXiv preprint math/0005003. 2000.
[41] Wattanasakulpong N, Mao Q. Dynamic response of Timoshenko functionally graded beams with classical and non-classical boundary conditions using Chebyshev collocation method. Compos Struct. 2015;119:346-54.
[42] Şimşek M. Fundamental frequency analysis of functionally graded beams by using different higher-order beam theories. Nucl Eng Des. 2010;240:697-705.
[43] Wu J, Zhang Y, Chen L, Luo Z. A Chebyshev interval method for nonlinear dynamic systems under uncertainty. Appl Math Model. 2013;37:4578-91.